Scientific Reports

https://doi.org/10.1038/s41598-026-45270-1

Article in Press

Structural, optical and luminescence properties of Fe^{3+}-doped mixed alkali zirconia-borate glasses for warm orange-red photonic applications

Received: 21 February 2026

Accepted: 17 March 2026

Published online: 26 March 2026

Cite this article as: Vinay D., Devaraja C., Deka U. *et al.* Structural, optical and luminescence properties of Fe^{3+}-doped mixed alkali zirconia-borate glasses for warm orange-red photonic applications. *Sci Rep* (2026). https://doi.org/10.1038/s41598-026-45270-1

D. Vinay, C. Devaraja, Utpal Deka & R. S. Gedam

Structural, Optical and Luminescence Properties of Fe^{3+}-Doped Mixed Alkali Zirconia-Borate Glasses for Warm Orange-Red Photonic Applications

Vinay D[1], Devaraja C[1*], Utpal Deka[2*] R.S. Gedam[3]

[1] Department of Physics, Manipal Institute of Technology Bengaluru, Manipal Academy of Higher Education, Manipal, Karnataka, 576104, India.

[2] Department of Physics, Sikkim Manipal Institute of Technology, Sikkim Manipal University, Majhitar, East Sikkim, 737136, India

[3] Department of Physics, Visvesvaraya National Institute of Technology, Nagpur- 440010, Maharashtra, India.

* Corresponding author. devaraja.c@manipal.edu, utpal.d@smit.smu.edu.in

Abstract:

A novel series of Fe^{3+} doped mixed alkali zirconia-borate glasses with the composition $60B_2O_3$ - $25Na_2O$ - $10Li_2O$ - (5-x) ZrO_2 - x Fe_2O_3 (x = 0 mol% – 1 mol%) were synthesized using the melt-quenching technique. The novelty of this work lies in combining the structural modifications with enhanced optical properties and orange-red luminescence in Fe^{3+} doped mixed alkali zirconia-borate glasses for warm photonic applications. X-ray diffraction confirmed the non-crystalline nature of glass, while SEM images and EDS spectra were utilised for morphological and elemental analysis. The density of the glasses decreased from 2.4197 $g.cm^{-3}$ to 2.4168 $g.cm^{-3}$ before gradually increasing to 2.4324 $g.cm^{-3}$. FTIR and Raman spectral studies showed the formation of non-bridging orthoborate units from pentaborate and di-pentaborate units. The optical absorption band at 450 nm is associated with the Fe^{3+} transition $^6A_{1g}$ (^6S) → $^4A_{1g}$ (^4G); ^4E_g (^4G). The decrease in direct bandgap from 3.90 eV to 3.10 eV and indirect bandgap from 3.44 eV to 2.77 eV, along with an increase in Urbach energy from 0.245 eV to 0.273 eV, indicates the disorder in structure. An

increase in refractive index leads to an increase in third-order susceptibility and nonlinear refractive index. The photoluminescence spectra exhibited orange-red emission at ($^4T_{2g}(^4G) \rightarrow {}^6A_{1g}(^6S)$) with 550 nm, 560 nm and 570 nm excitation wavelengths. The CIE chromaticity and CCT values show that Fe^{3+} doped glasses are suitable for warm-emitting orange-red photonic applications.

Keywords:

Fe^{3+}-doped borate glasses; Melt-quenching technique; Optical bandgap and Urbach energy; Nonlinear optical properties; Orange-red photoluminescence.

Introduction

Advanced glass materials are developing as a major emphasis in material science due to their diverse structural and optical features, which allow for a wide range of industrial and technological applications. Among these materials, glasses have become ubiquitous and flexible because of their inherent benefits, which include easy doping with different elements for modifying their properties, cost-effectiveness in fabrication, and simple processing methods [1,2]. In modern applications, the potential of an assortment of glass-forming systems, including borosilicate [3,4], tellurite [5], silicate [6], phosphate [6], boro-tellurite [7], vanadate [8], and chalcohalide glasses [9], has been extensively investigated. Borate-based glasses have drawn a lot of interest in the field since their recent developments, like smart lighting technologies, and next-generation display devices, due to their distinctive arrangements in the structure, low melting points, non-toxicity, thermal and chemical stability [10,11]. Energy-saving devices [12], laser media [13], thermal and UV sensing, optoelectronic modulators [11], and photonic applications [14,15] are a few recent advancements in these glasses.

The distinct structure of B_2O_3 in the glass network substantially determines the special features of the borate glasses. The two coordination

states of B_2O_3 are BO_3 (trigonal) units and BO_4 (tetrahedral) units, which will link to form the boroxol rings (B_3O_6), and other structures like metaborate, pyroborate, and other structures. These linkages of BO_3 and BO_4 units form bridging oxygens (BOs) in the glassy network. Inclusion of alkali oxides like Li_2O, Na_2O, into the glass structures initially forms BOs. Furthermore, high concentrations of alkali oxides act as modifiers by breaking the network, forming non-bridging oxygens (NBOs) in the network, and this process is called the borate anomaly [16–18]. Thus, the modification of the network will directly impact on structural, physical, and optical properties of the glasses due to the variation in the ratio of BOs to NBOs units in the network of the glass [19,20].

Transition metal oxides in borate glass act as dopants, modifying the structural and optical properties for advancements in electro-optical devices. ZrO_2 with the +4-oxidation state contributes to the glass in network formation with [ZrO_4] and [ZrO_6] units [21]. The presence of ZrO_2 in the glass matrix can improve the fragility and thermal stability of the glass [21,22]. Similarly, Fe_2O_3 with various oxidation states, Fe^{3+} (ferric) and Fe^{2+} (ferrous), exhibits [FeO_4] and [FeO_6] units with tetrahedral and octahedral domains where Fe^{3+} occupies both the domain and Fe^{2+} occupies only in octahedral domain [23]. The stable state of Fe_2O_3 is the Fe^{3+} (trivalent) state, which develops a spin-forbidden transition with a weak absorption band near 400 nm – 500 nm. The presence of an ionic state improves the ligand field; in addition, it illuminates the colour and improves the optical features of the host glass [24]. The illumination in luminescence of the Fe_2O_3-doped glass can change to various regions in the CIE colour coordination as the glass is converted into glass ceramics [25].

Huang Q et al. [25] studied the effect of Fe_2O_3 doped in magnesium alumino-silicate-based glasses. The addition of Fe_2O_3 showed an increase in NBOs. Optical spectra reveal the presence of Fe^{2+} and Fe^{3+} in glass and an increase in the ionic nature of the glass. Photoluminescence spectra showed dark blue emission due to Fe^{3+} transitions in glass. V Pattar et al.

[26] examined the iron oxide-doped sodium boro-tellurite glasses. The existence of Fe^{3+} was shown in EPR spectra, and the formation of BO_3 units from BO_4 units was recorded. Optical properties were calculated and compared with the change in structure in the glass network. Youli Xu et al. [27] discussed the impact of radioactive nuclear waste Fe_2O_3 in Mo-borosilicate glass. Homogeneity in the structure was seen above 3.85 mol%, and the addition of Fe_2O_3 contributes towards network formation. The incorporation of iron oxides improved the chemical durability of the sample.

Problem Statement: The ability of Fe^{3+} doped borate glasses to alter the optical and structural characteristics of the glass network has gained significant interest. Incorporating Fe^{3+} into mixed alkali zirconia borate glasses can alter borate structural units and create localised electronic states that impact optical absorption and luminescence. Fe^{3+} doped mixed alkali zirconia borate glasses have promising characteristics for electro-optical and photonic applications. Understanding the role of Fe^{3+} ions in influencing the structural and optical properties of this glass system is an essential research problem.

Research Gap: Although Fe^{3+} based borate glasses have been thoroughly examined for their structural and optical properties, Fe^{3+}-doped mixed alkali zirconia-borate glasses are comparatively unexplored, particularly for their orange-red luminescence and non-linear optical response from the optical bandgap. The relationship between structural modification of borate units and the consequent optical and luminescence properties has not been extensively explored. Moreover, limited investigations have studied the influence of Fe^{3+} inclusion on nonlinear optical characteristics such as nonlinear refractive index and third-order susceptibility in these glass systems. Therefore, a detailed investigation linking structural modifications and optical luminescent properties is necessary to evaluate their potential for photonic applications.

Current Research Focus: In agreement with earlier literatures, mixed alkali zirconia borate glasses doped with Fe_2O_3 are not explored much with

orange-red emission, electro-optical and photonic applications. The current study focused on novel glass systems with a matrix of $60B_2O_3$ - $25Na_2O$ - $10Li_2O$ - (5-x) ZrO_2 - x Fe_2O_3, with x = 0.0 to 1.0 mol%, synthesised while taking into consideration the abovementioned challenges. The physical, structural, optical and photoluminescence characteristics were investigated for potential applications in electro-optical and photonic applications.

Experimental Details

Sample Preparation

The novel glass series with the composition $60B_2O_3$ - $25Na_2O$ - $10Li_2O$ - (5-x) ZrO_2 - x Fe_2O_3, x = 0.0, 0.2, 0.4, 0.6, 0.8, 1.0 mol%, was synthesised using the melt quenching technique. The synthesised glass system is coded as BNLZF-00, BNLZF-02, BNLZF-04, BNLZF-06, BNLZF-08, and BNLZF-10 and tabulated in **Table 1**. The inorganic and basic ingredients are composed of boric acid, sodium carbonate, lithium carbonate, zirconium carbonate, and ferric sulphate from Sigma Aldrich, with 99% purity, with AR grade. The chemicals were weighed precisely according to the stoichiometric ratio, and all the chemicals were grinded in an agate mortar and pestle for about 30 minutes to achieve homogeneity in the mixture. The well-grinded mixture is filled inside the porcelain crucible and placed in the muffle furnace. The temperature is set for 1100 °C and held for 30 minutes. The melt in the crucible is stirred to ensure homogeneity and quenched on the brass rectangular plate, which consists of steel rings placed on it and is pressed with the brass mould on the super-cooled liquid. The synthesis procedure is illustrated in **Figure 1**. The prepared glass samples were stored in the desiccator to prevent airborne moisture to the samples. Furthermore, the samples were crushed to get the powder, and round pellet-shaped samples were polished with sandpaper graded from 320 to 2000 microns to perform further characterisations.

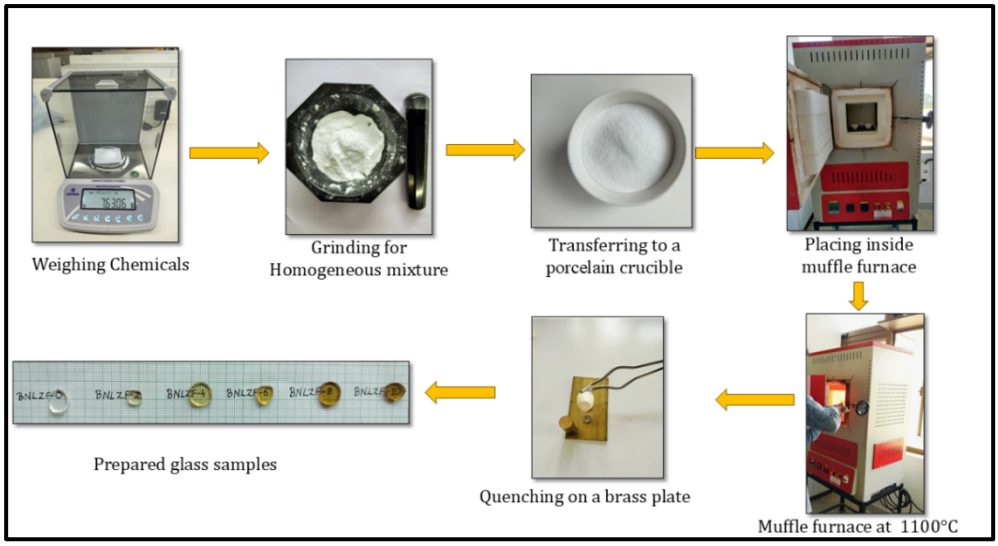

Figure 1: Synthesis of BNLZF glasses by the melt quenching technique.

Table 1: Chemical Composition of the glass.

Sample Composition					
Sample Code	B_2O_3 mol%	Na_2O mol%	Li_2O mol%	ZrO_2 mol%	Fe_2O_3 mol%
BNLZF-00	60	25	10	5.0	0.0
BNLZF-02	60	25	10	4.8	0.2
BNLZF-04	60	25	10	4.6	0.4
BNLZF-06	60	25	10	4.4	0.6
BNLZF-08	60	25	10	4.2	0.8
BNLZF-10	60	25	10	4.0	1.0

Sample Characterization

The X-ray diffraction (XRD) analysis of the powder sample was carried out using an XRD RIGAKU equipped with a 6000-type diffractometer with a Cu radiation source (λ =1.541 Å). The instrument was operated at the tube voltage of 40kV and a tube current of 30mA. The diffraction data were collected over a 2θ range of 10° – 80° at a scanning rate of 4° per minute. The morphological and elemental configuration of the glass samples is examined using the ZEISS EVO 10 Scanning Electron Microscope (SEM), which has an Element Energy Dispersive Spectroscopy (EDS) system with an additional backscattered electron detection. To minimize the effects of the charges generated by the beam of an electron, a thin layer of Au sputtering was required to coat on the sample surface. An ATIR-FTIR spectrometer is used to record the infrared absorption spectra of fine powdered samples at room temperature, ranging from 400 cm^{-1} to 1600 cm^{-1}. A confocal Raman microscope of Horiba Jobin Yvon-Xplora plus V2.1 multiline is scanned in the range from 50 cm^{-1} to 1600 cm^{-1} at room temperature to obtain the Raman spectra. The resulting absorption spectra are deconvoluted to resolve the peaks. The deconvolution of FTIR spectra and Raman spectra, band fitting was carried out using an ancillary software “Origin 2024b”, with a “Gaussian fit” of deconvolution in a built-in function “Multiple Peak fit” of absorption spectra for prepared samples. The R^2 (fitting parameter) values were found to be 0.99, which is equal to 1, with the error rate of ±0.001. The density of the synthesised samples was ascertained using Archimedes’ buoyancy effect at room temperature, with distilled water as the suspension medium. Using a Shimadzu UV-1900I model spectrometer, UV-Vis absorption spectra were obtained at room temperature. The refractive index of the glass was measured using a Gemology Gemstone Gem Refractometer using a Monochromatic Light Filter with a minimum gradation value: 0.01 RI. The photoluminescence spectra are obtained using Horiba Jobin Yvon using the FL-1039/40 model with a 200 nm – 900 nm wavelength range at room temperature, with an excitation wavelength of 425 nm and emission wavelength of 600 nm.

Results and Discussion

X-ray diffraction (XRD)

The XRD patterns of the BNLZF glass series are displayed in **Figure 2.** The scanning angle 2θ (deg) ranges from 10° to 80°, and the absence of sharp peaks indicates the non-crystalline nature of the glass structure. The broad bands observed at 15°-25°, and 25°-40° are due to the presence of Li^+ and Na^+ alkali ions in the borate structure, creating short-range disordered structures, and the 40°-55° broad hump with low intensity is due to the presence of ZrO_2 with the borate structure. These broad humps indicate the short-range disorders in the glassy network [28–30].

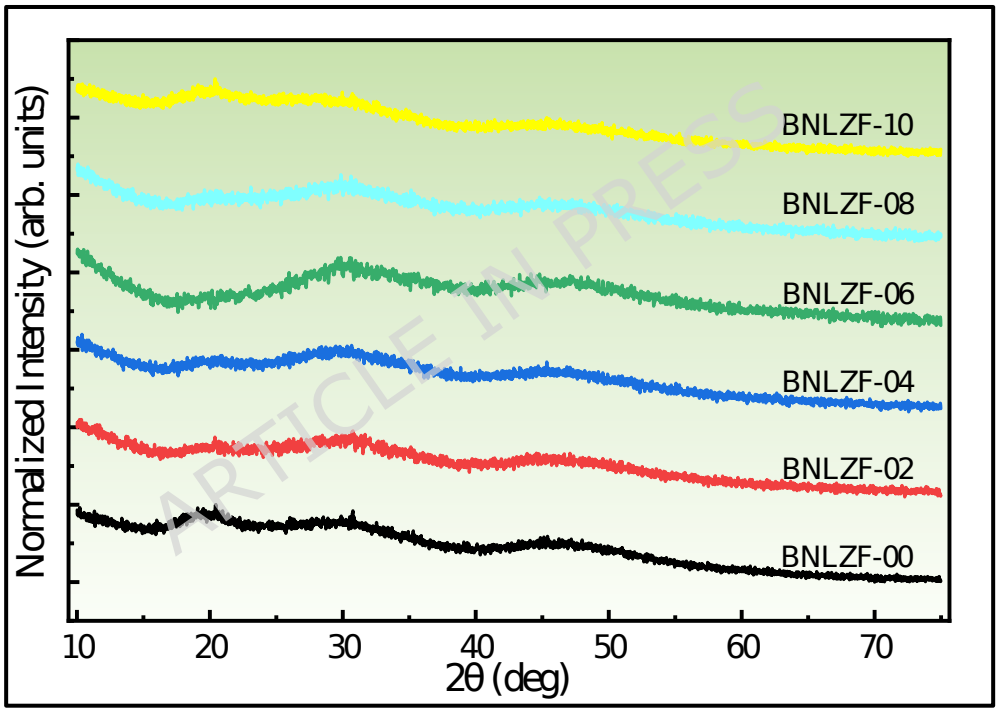

Figure 2: XRD spectra of BNLZF glasses.

SEM and EDS

To obtain morphological analysis on the surface level and find the composition of elements is crucial for material characterisation by using SEM images and EDS spectra. **Figure 3** shows the images of SEM of the BNLZF glasses, where the particles were subjected to a high vacuum and magnified at a 10.00 KX level. Powder of the glass is noticeable in the

images as small, tiny particles amidst a specific size in a few hundred nm ranges. It is feasible to detect amorphous nature in the chemical configurations on these nanometric dust particles that lack an ordered crystal structure in 10.00 KX magnification. The EDS spectra of the BNLZF glass series are shown in **Figure 4**. The increase in the peak of Fe is seen as the concentration of Fe_2O_3 has been introduced from BNLZF-02 to BNLZF-10 glass samples. The presence of B, Na, Li, Zr, Fe and O peaks confirms the occurrence of the elements in the glass structure. Nevertheless, based on the region that was measured, the weight percentage and the atomic percentage values in the data gathered from the spot of EDS spectra do not show a regular distribution. This further demonstrates that the structure is not entirely homogeneous [31]. The gold sputtering process on glass samples caused an additional peak between 1.34 and 2.01, representing the presence of Au. The lack of foreign elements indicated in the spectra provides the information of no extraneous materials from the crucible were contained in the glass samples [32–35].

a.

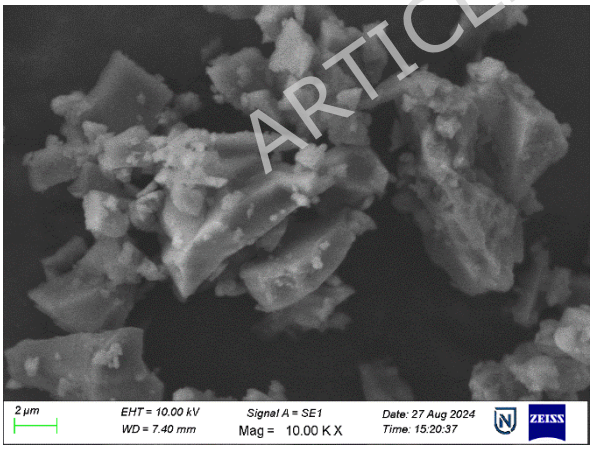

b.

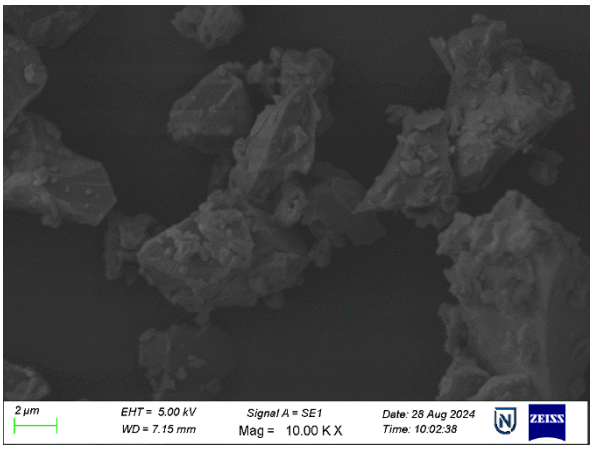

c.

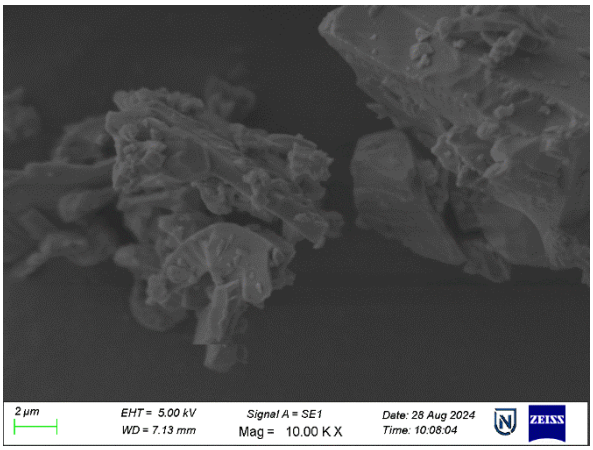

d.

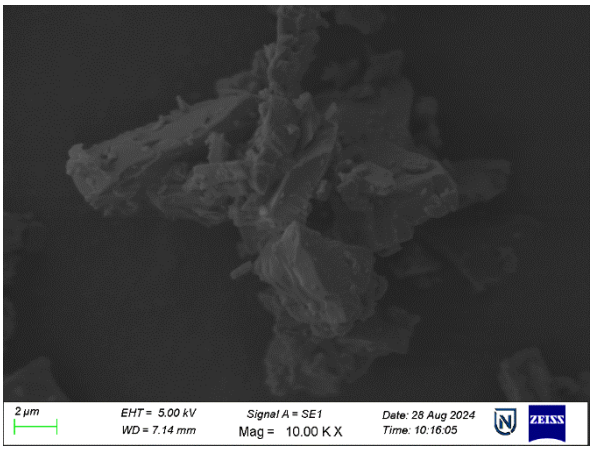

e.

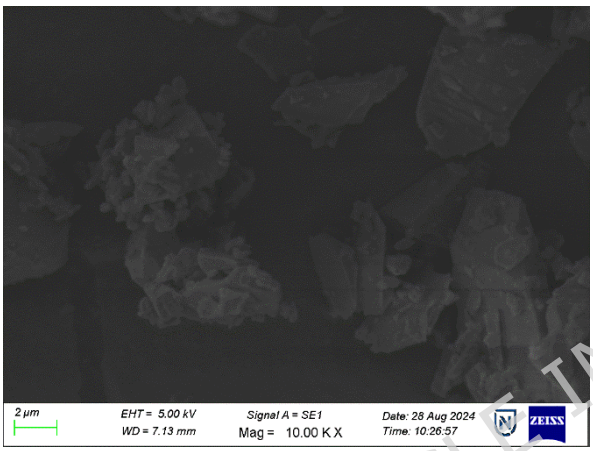

f.

Figure 3: (a-f). SEM images of BNLZF glasses.

a.

BNLZF-00

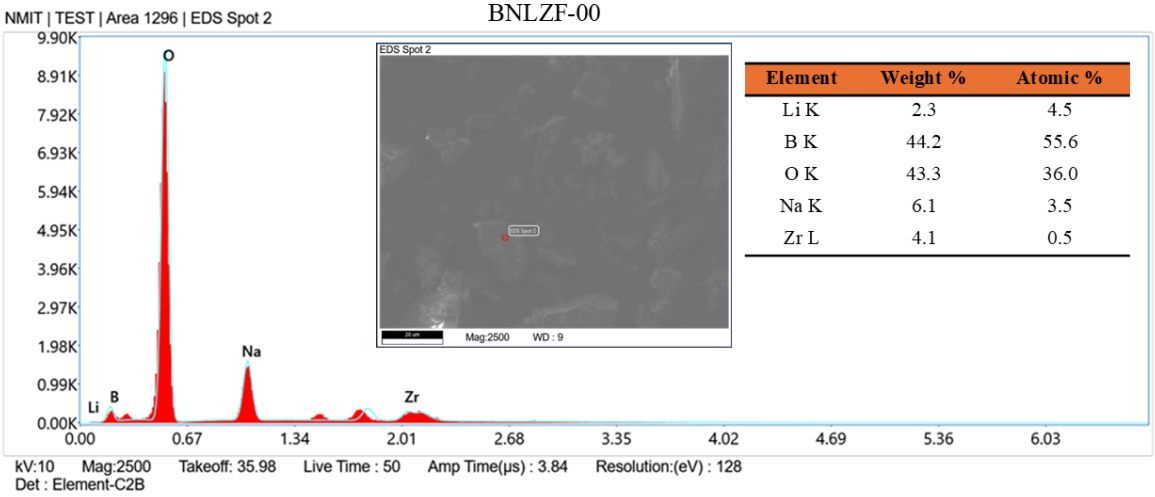

Element	Weight %	Atomic %
Li K	2.3	4.5
B K	44.2	55.6
O K	43.3	36.0
Na K	6.1	3.5
Zr L	4.1	0.5

b.

BNLZF-02

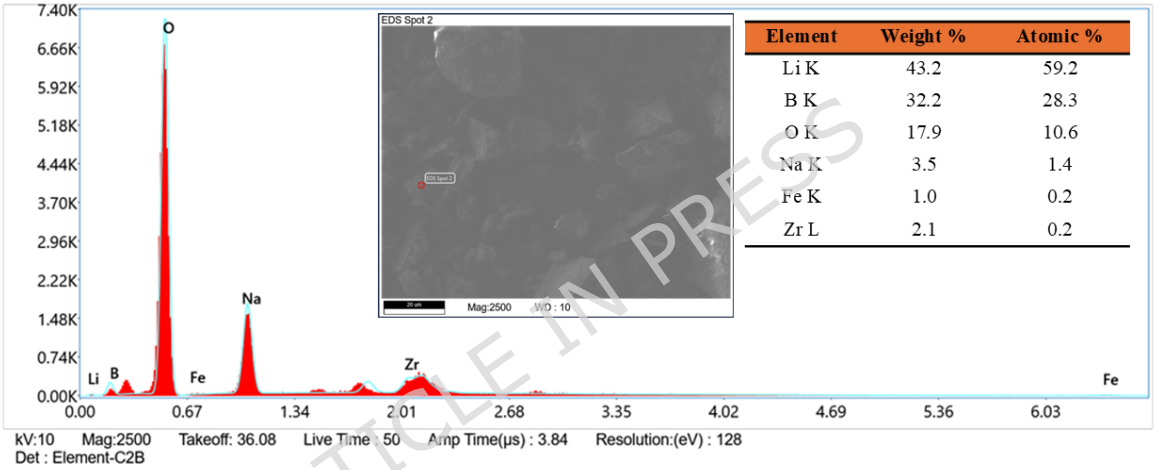

Element	Weight %	Atomic %
Li K	43.2	59.2
B K	32.2	28.3
O K	17.9	10.6
Na K	3.5	1.4
Fe K	1.0	0.2
Zr L	2.1	0.2

c.

BNLZF-04

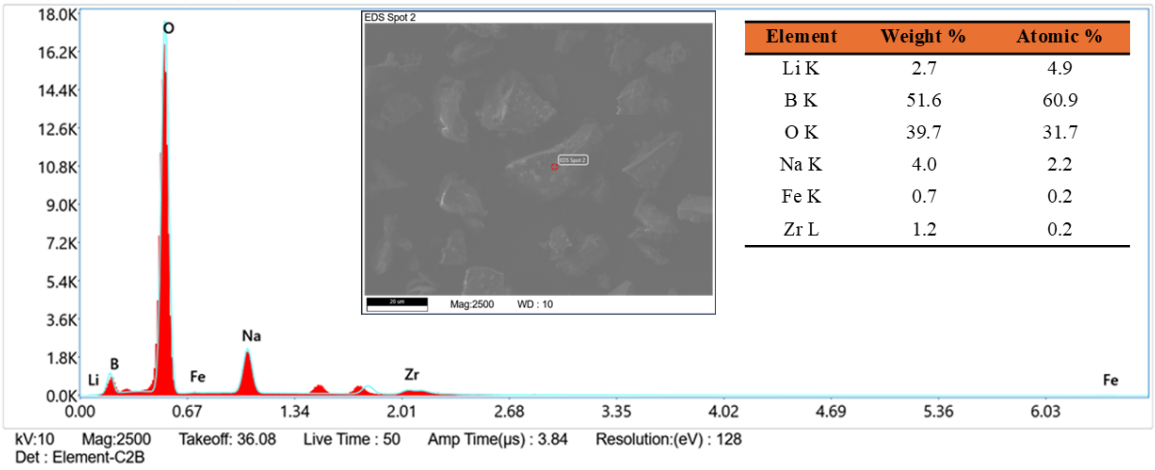

Element	Weight %	Atomic %
Li K	2.7	4.9
B K	51.6	60.9
O K	39.7	31.7
Na K	4.0	2.2
Fe K	0.7	0.2
Zr L	1.2	0.2

d.

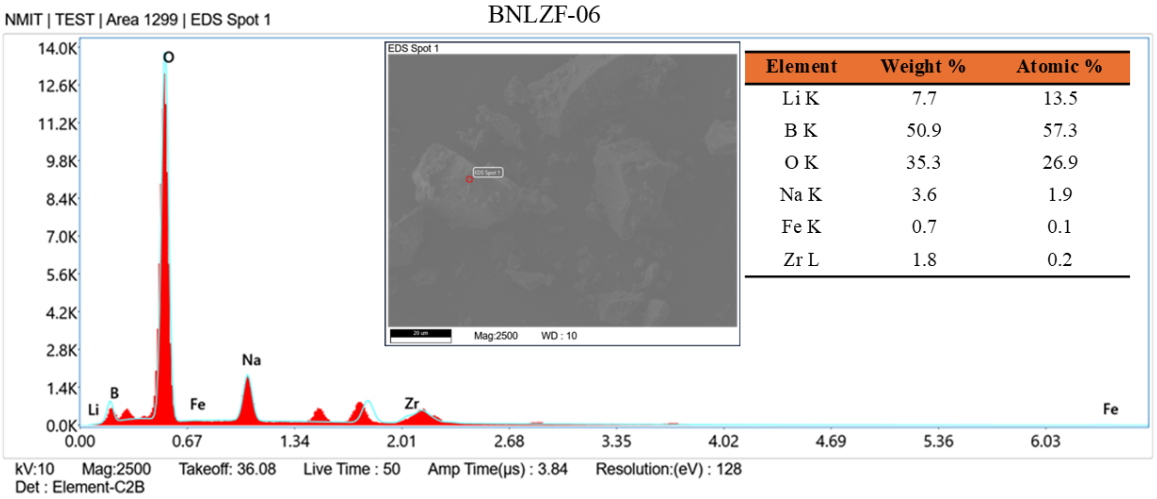

Element	Weight %	Atomic %
Li K	7.7	13.5
B K	50.9	57.3
O K	35.3	26.9
Na K	3.6	1.9
Fe K	0.7	0.1
Zr L	1.8	0.2

e.

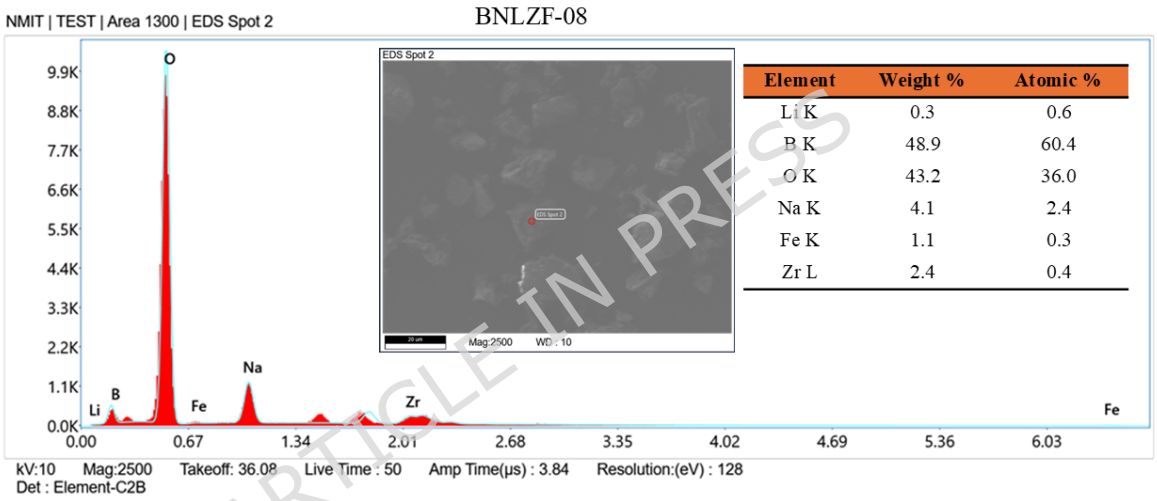

Element	Weight %	Atomic %
Li K	0.3	0.6
B K	48.9	60.4
O K	43.2	36.0
Na K	4.1	2.4
Fe K	1.1	0.3
Zr L	2.4	0.4

f.

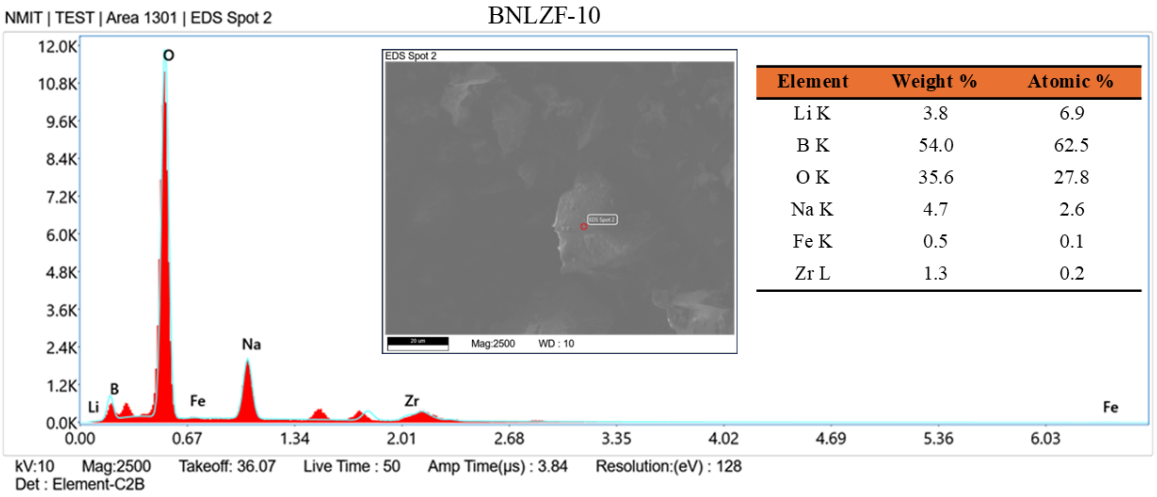

Element	Weight %	Atomic %
Li K	3.8	6.9
B K	54.0	62.5
O K	35.6	27.8
Na K	4.7	2.6
Fe K	0.5	0.1
Zr L	1.3	0.2

Figure 4: (a-f). EDS spectra of BNLZF glasses.

Physical Properties

The physical properties of BNLZF glasses, including molar volume (V_M), molar volume of boron (V_m^B), average boron-boron distance ($d_{<B-B>}$), oxygen molar volume (V_O), oxygen packing density (OPD), transition metal ion (TMI) concentration (N_{Fe}), inter-ionic distance (r_{Fe}), polaron radius (r_p), and field strength (F) was calculated based on the molecular weight (M_W) and density (ρ) values of glass samples. The corresponding calculated values were listed in **Table 2**.

Density is a vital characteristic that can be used effectively to examine variations in structures within the glass system. It functions as an essential measurement of the internal structures and atomic packing of a material. The degree of compactness, the size of interstitial voids, the geometrical structures of structural units, and the individual atoms' coordination number are key variables in determining the glass density. In this work, the density of the glass samples was evaluated using a laboratory setup built on Archimedes' principle. **Equation 1** is used to measure the density of the glass samples and is tabulated in **Table 2**.

$$\rho = \frac{w_a}{w_a - w_d}\rho_d \quad (1)$$

where ρ_d is the density of the distilled water = 1.0 gcm^{-3}, w_a is the weight of the glass samples in air, and w_d is the weight of the glass samples in liquid [36].

The V_M of the glass is determined using **equation 2**. The computed values are displayed in **Table 2**.

$$V_m = \frac{M_w}{\rho} \quad (2)$$

$$V_m^B = \frac{V_m}{2(1-X_B)} \quad (3)$$

$$d_{<B-B>} = \left(\frac{V_m^B}{N_A}\right)^{\frac{1}{3}} \quad (4)$$

$$V_O = \frac{V_m}{\Sigma_i (x n_o)_i} \quad (5)$$

$$OPD = \frac{1000 \times \sum_i (xn_0)_i}{V_m} \quad (6)$$

$$N_{Fe} = \frac{N_A \times \text{mol\% of cation} \times \text{valance of cation}}{V_m} \quad (7)$$

$$r_{Fe} = \left(\frac{1}{N_{Fe}}\right)^{1/3} \quad (8)$$

$$r_p = \frac{1}{2}\left(\frac{\pi}{6N_{Fe}}\right)^{\frac{1}{3}} \quad (9)$$

$$F = \frac{Z}{(r_p)^2} \quad (10)$$

Where, M_w is the molecular weight of BNLZF glasses, X_B is B_2O_3 mol% in BNLZF glasses, xn_0 is the mole fraction of the composition with the number of oxygens in the mole fraction, N_A is Avogadro's number, Z valency of cation doped in the BNLZF glasses [36–38].

Figure 5 shows the variation in the density and molar volume of all BNLZF glasses. As ρ increases from 2.4197 g.cm^{-3} to 2.4324 g.cm^{-3} the V_m also increases from 47.8548 cm^3.mol^{-1} to 49.2568 cm^3.mol^{-1} along with it, as shown in **Table 2**. At 0.2 mol% of Fe_2O_3 replacing ZrO_2, ρ reduces to 2.4168 g.cm^{-3} due to the presence of Fe^{2+} and Fe^{3+} with the ionic radii of 0.077 nm and 0.064 nm, respectively [39], in the tetrahedral and octahedral sites inside the glass network between the small amount of zirconium and the large amount of borate structures. Furthermore, the higher molecular weight of the Fe_2O_3 (159.69 g/mol) compared to the molecular weight of the ZrO_2 (123.218 g/mol) leads to an increase in ρ. V_m behaves in a similar pattern to that of ρ, which can be presumed with the following explanations: (i) the increase in oxygen number, where Fe_2O_3 has a greater number of oxygens than ZrO_2. (ii) The V_m of Fe_2O_3 (41.52 cm^3.mol^{-1}) is greater than V_m of ZrO_2 (20.849 cm^3.mol^{-1}). (iii) Formation of NBOs as described in the FTIR and Raman section [39,40].

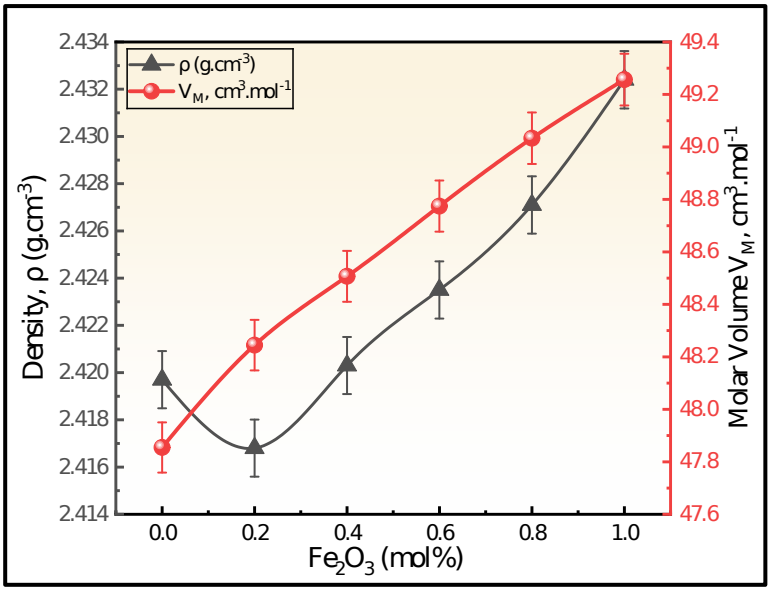

Figure 5: Density and molar volume plot of the BNLZF glasses.

V_O^B has increased from 5.9819 × 10^{-5} $m^3.mol^{-1}$ to 6.1571 × 10^{-5} $m^3.mol^{-1}$, and an increase in $d_{<B-B>}$ from 4.6313 Å to 4.6760 Å as the concentration of the iron is replaced with zirconium. This results in the replacement of Fe^{3+} ions, which has increased the boron distance in the glass network [39].

The V_O has increased since the trend of OPD is in the reverse direction was recorded as seen in **Figure 6.** Therefore, the addition of iron oxide has been shown to increase in NBOs within the molecular structure of the network of the glass. The V_O in the glass structure has increased from 21.2866 cm^3 to 21.7950 cm^3 and OPD decreased to 45.8820 g.atom/l from 47.0172 g.atom/l. The addition of Fe_2O_3 had a sensitive effect upon the way the oxygen molecules inhabited the vacant space inside the molecular structure of the glass network, causing this change in OPD. These two physical characteristics are known to be related to the quantity of oxygen atoms adorned within the molecular structure of the glass network. In the molecular structure of the glass, the oxygen has a larger ionic radius than the other components (O^{2-}: 0.140 nm, B^{3+}: 0.020 nm, Na^+: 0.102 nm, Li^+: 0.076 nm, Zr^{4+}: 0.080 nm, Fe^{2+}: 0.077 nm, and Fe^{3+}: 0.064 nm). This

evidence indicates that the addition of the Fe^{3+} affects both the molar and free volumes of the glassy network [41].

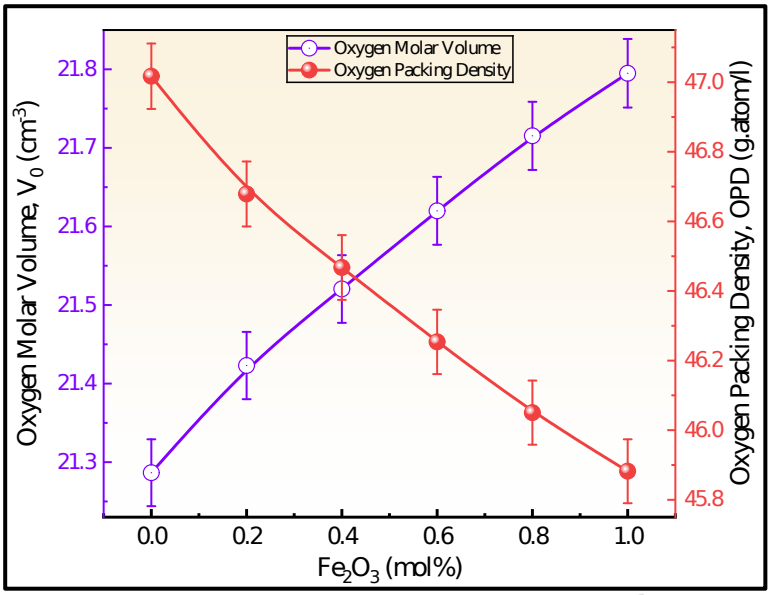

Figure 6: V_O and OPD plot of the BNLZF glasses.

Furthermore, an increase in the concentration of Fe_2O_3, the ionic concentration of Fe^{3+} (N_{Fe}) increased from 0.7489 × 10^{20} ions/cm^3 to 3.6677 × 10^{20} ions/cm^3 in the glass structure. Furthermore, field strength has increased from 3.2812 cm^{-2} to 9.4623 cm^{-2}, enhancing the exerted electrostatic force from the Fe^{3+} ions on the surrounding oxygen ions in the glass network. However, the inter-ionic distance (r_{Fe}) and polaron radius (r_p) increased from 2.3724 nm to 1.3970 nm and 9.5620 Å to 5.6307 Å, respectively, as shown in **Figure 7**. This reduces the distance between the Fe^{3+} ions and improves the distortion in the glass by the localised charge carriers within the glassy network [26,40].

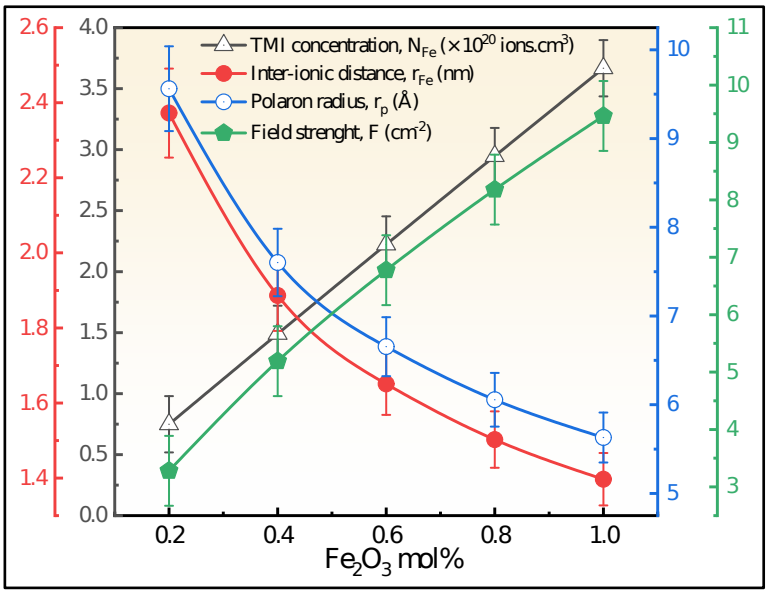

Figure 7: Comparison of N_{Fe}, r_{Fe}, r_p and F plot of the BNLZF glasses.

Table 2: The physical properties of the BNLZF glasses (All the parameters are calculated with an error range of ±0.001).

Glass code	BNLZF-00	BNLZF-02	BNLZF-04	BNLZF-06	BNLZF-08	BNLZF-10
M_W, g.mol^{-1}	115.7943	116.5978	117.4014	118.2050	119.0085	119.8121
ρ, g.cm^{-3}	2.4197	2.4168	2.4203	2.4235	2.4271	2.4324
V_M, cm^3.mol^{-1}	47.8548	48.2447	48.5070	48.7745	49.0332	49.2567
V_O^B, × 10^{-5} m^3.mol^{-1}	5.9819	6.0306	6.0634	6.0968	6.1292	6.1571
$d_{<B-B>}$, Å	4.6313	4.6438	4.6522	4.6607	4.6690	4.6760
V_O, cm^3	21.2866	21.4230	21.5204	21.6199	21.7153	21.7950
OPD, g.atom/l	47.0172	46.6787	46.4676	46.2537	46.0504	45.8820
N_{Fe}, × 10^{20} ions/cm^3	0	0.7489	1.4898	2.2224	2.9476	3.6677
r_{Fe}, nm	0	2.3724	1.8864	1.6509	1.5026	1.3970
r_p, Å	0	9.5620	7.6031	6.6541	6.0563	5.6307
F, cm^{-2}	0	3.2812	5.1897	6.7756	8.1791	9.4623

Fourier Transform Infra-Red (FTIR) Spectroscopy Analysis

FTIR spectroscopy is categorized as vibrational spectroscopy, and it is a sensitive and non-destructive method for examining the arrangements of the structural components in the matrix of the glass system. FTIR absorption spectra indicate numerous peaks of BNLZF glasses in distinct vibrations of the elements in the glass matrix, including B_2O_3, Na_2O, Li_2O, ZrO_2, and Fe_2O_3. **Figure 8** displays the FTIR spectra of the synthesized glasses in the range of 400 cm^{-1} to 1600 cm^{-1}. As seen in the figure, the spectra contain four regions: (i) 400 cm^{-1} – 600 cm^{-1} attributed to metallic cations vibration, (ii) 600 cm^{-1} – 800 cm^{-1} accredited to B-O-B and Zr-O-Zr bending vibrations, (iii) 800 cm^{-1} – 1200 cm^{-1} is ascribed to symmetrical and asymmetrical vibrations of BO_4 units, and (iv) 1200 cm^{-1} – 1600 cm^{-1} is endorsed to asymmetrical vibrations of BO_3 units [42,43]. **Table 3** lists the detected bands and their related band assignments. The deconvoluted spectra are displayed in **Figure 9**.

The observable broadband near ~ 476 cm^{-1} is assigned to (i) cationic vibrations of (Na^+, Li^+, Zr^{4+}, Fe^{3+}, (ii) octahedron $[ZrO_6]^{2-}$ vibrations, (iii) vibrations of octahedral units of FeO_6 [44–47]. A small band ~ 500 cm^{-1} representing the stretching vibration of ZrO_4 units. The band at ~ 450 cm^{-1} has shifted to ~ 476 cm-1 as Fe_2O_3 replaced ZrO_2 in the glass structure. Furthermore, the band at ~ 500 cm^{-1} converges with the band at ~ 476 cm^{-1}, resulting in the reduction of ZrO_4 units in the glass, which replaces FeO_4 tetrahedral and FeO_6 octahedral units in the glass network [45,48]. The peak ranging ~704 cm^{-1} - ~ 706 cm^{-1} represents bending vibrations of B-O-B linkages in borate two triangular series [O_2B-O-BO_2] with Zr-O-Zr linkages in ZrO_4 units. However, as the concentration of Fe_2O_3 increases, the ZrO_4 units will replace the vibration of Fe-O bonds in FeO_4 units in the glassy network [34,45,48]. The peak ~ 823 cm^{-1} – ~ 838 cm^{-1} and ~ 863 cm^{-1} – ~ 888 cm^{-1} attributed to B-O-B bending of tri-, tetra- and penta-borate units [48,49]. The more intense bands ~ 926 cm^{-1} – ~ 947 cm^{-1} and ~ 992 cm^{-1} – ~ 1006 cm^{-1} are tailored to diborate units [$B_4O_7^{2-}$] of BO_4 or [$BØ_4$]$^-$ groups, where Ø denotes bridging oxygen (BO) and O^- denotes non-

bridging oxygen (NBO_S) in the glass network [46,49,50]. The peaks ~ 1065 cm^{-1} – ~ 1075 cm^{-1} are ascribed to stretching vibrations of various (tri-, tetra- and penta-) borate groups in BO_4 units [51]. The BO_3 groups create boroxol rings ($B_3O_{4,5}$).BO_4 groups can be integrated into a variety of boroxol groups, forming from di-, tri-, tetra, and penta-borate groups into ortho-, meta-, and pyro-borate groups. The small shoulder bands ~ 1226 cm^{-1} – ~ 1236 cm^{-1} are attributed to the formation of BO_3^{3-} (ortho-borate) units [49]. The intense peaks ~ 1307 cm^{-1} - ~ 1309 cm^{-1} are imputed to the formation of $B_2O_5^{4-}$ (pyro-borate dimers) in the network of the glass [52]. The band ~ 1378 cm^{-1} – 1392 cm^{-1} is ascribed to the stretching vibration of $B\text{-}O^-$ in $BØ_2O^-$ (meta-borate) units. The smaller shoulder peaks ~ 1462 cm^{-1} - ~ 1482 cm^{-1} represent the asymmetric stretching vibrations of B-Ø in $BØ_3$ units [52,53].

The contraction of the BO_4 units concerning the broadening of the BO_3 units is seen in the spectra from BNLZF-00 to BNLZF-10 glasses. Major reduction of the intensity of diborate and pentaborate units from BNLZF-00 to BNLZF-10 with an increase in intensity of ortho-borate (BO_3^{3-}) units, and the shift in peaks is observed in the deconvoluted spectra. This explains the conversion of diborate and pentaborate units into ortho-borate units in the network of the glass as the concentration of the Fe_2O_3 is increased in the glass system. To sum up, an extra oxygen from Fe_2O_3, substituting the ZrO_2, has increased the density and the formation of BO_3^{3-} leads to the NBOs in the glass network with an open structure. This formation of NBOs was confirmed by calculating the N4 parameter, N4 = (area of BO_4 groups) / (area of BO_4 groups + area of BO_3 groups) [26,54], which explains the ratio of BO_4 and BO_3 groups in the glass network. The calculated N4 parameter values of BNLZF-00 to BNLZF-10 are 0.5837, 0.5709, 0.5630, 0.5464, 0.5206, and 0.4952, respectively. The constant decreases in N4 parameters explain the formation of NBOs in the glassy network, where BO_4 units are converting into BO_3 units.

Table 3: Band assignments of deconvoluted FTIR spectra of BNLZF glasses.

BNLZF-00	BNLZF-02	BNLZF-04	BNLZF-06	BNLZF-08	BNLZF-10	Band assignments	Ref.
704	706	703	706	706	706	Bending vibrations of B-O-B linkages with Zr-O-Zr linkages in ZrO_4 units. Fe-O bonds in FeO_4 units.	[34,45,48]
827	823	830	829	833	838	B-O-B bending of tri-, tetra- and penta-borate units.	[48,49]
871	863	877	876	882	888		
933	926	939	936	944	947	Diborate units $[B_4O_7^{2-}]$ of BO_4 or $[B\emptyset_4]^-$ groups.	[46,49,50]
995	992	1000	996	1004	1006		
1065	1065	1068	1066	1076	1075	Stretching vibrations of tri-, tetra- and penta-borate groups.	[51]
1232	1226	1234	1234	1235	1236	BO_3^{3-} (ortho-borate) units.	[49]
1309	1308	1309	1308	1307	1309	$B_2O_5^{4-}$ (pyro-borate dimers).	[52]

1380	1392	1380	1380	1378	1382	Stretching vibration of B-O$^-$ in BØ$_2$O$^-$ (meta-borate) units.	[52,53]
1464	1482	1462	1464	1462	1462	Stretching vibrations of B-Ø in BØ$_3$ units.	[52,53]

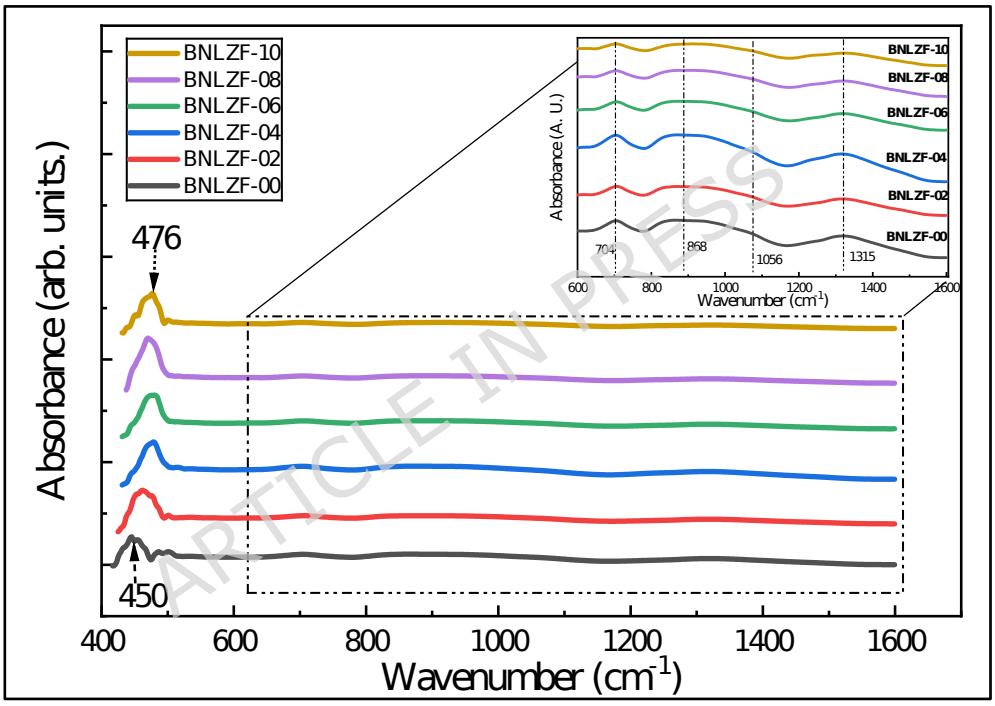

Figure 8: FTIR spectra of BNLZF glasses.

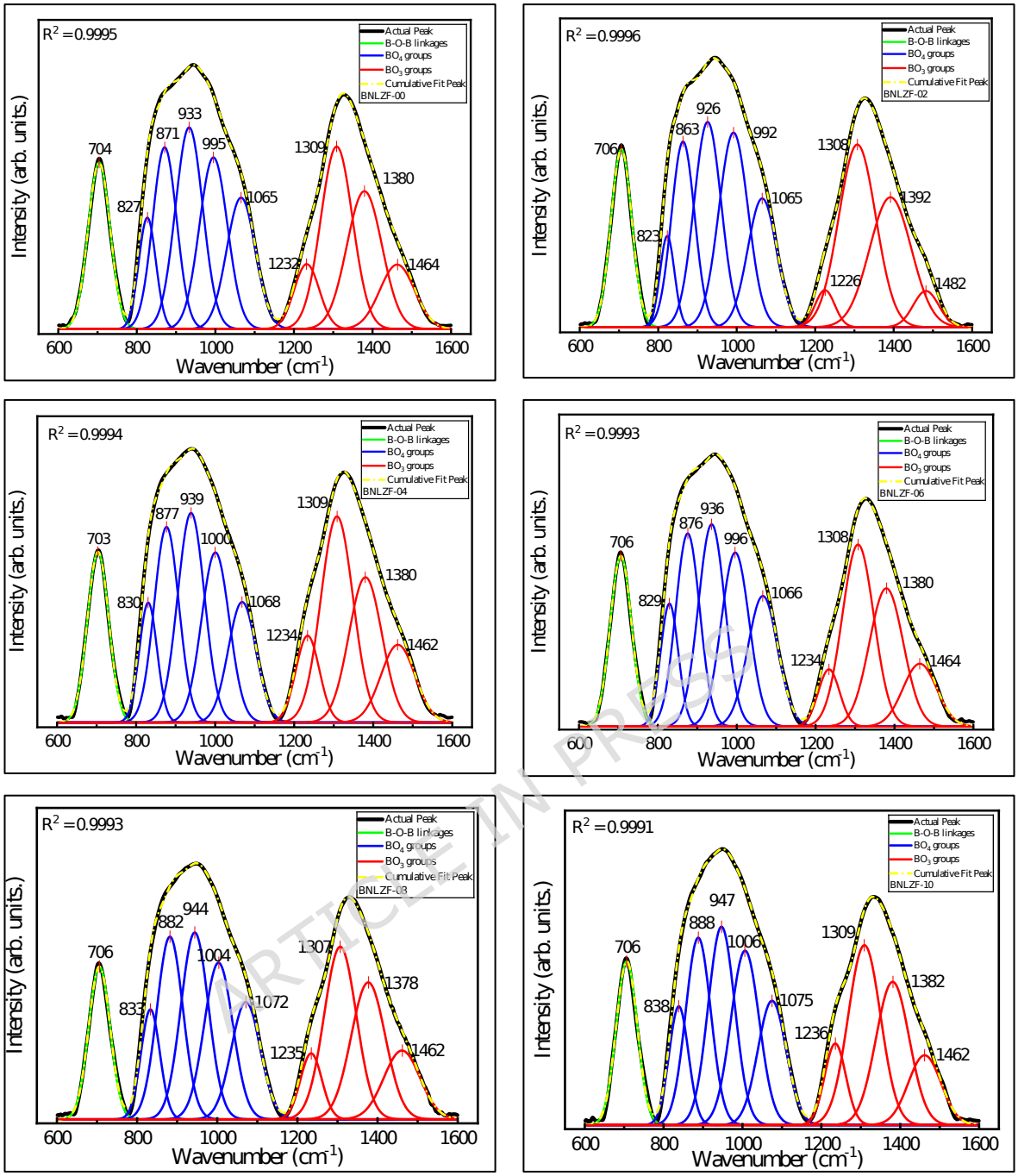

Figure 9: Deconvoluted FTIR spectra of BNLZF glasses.

Raman Spectroscopy

Raman spectroscopy is an effective method for examining the structural features of non-crystalline materials. This method thoroughly reveals the local atomic configurations and the impact of different dopants and modifiers on the glass structure. The Raman spectra of the BNLZF glasses were displayed in **Figure 10**. The deconvolution was conducted to identify

the band assignments and is illustrated in **Figure 11**, which is listed in **Table 4**. The bands have been separated into five sections for each of the synthesized glasses (i) < 200 cm^{-1}, (ii) 200 cm^{-1} – 400 cm^{-1}, (iii) 400 cm^{-1} – 800 cm^{-1}, (iv) 800 cm^{-1} – 1200 cm^{-1}, and (v) 1200 cm^{-1} – 1600 cm^{-1} [55].

The highest intensity band, ~ 126 cm^{-1}, referred to the boson peak due to the presence of alkali oxides (Li_2O and Na_2O) in the glass network [55,56]. The band between ~ 438 cm^{-1} to ~ 486 cm^{-1} is attributed to [ZrO_4] unit's vibrations in Zr-O linkages, and the bands ~ 481 cm^{-1} to ~ 564 cm^{-1} are assigned to the stretching of symmetrical bands of BO_4 units, which are surrounded by pairs of BO_3 units or the isolated diborate groups [49,56,57]. The strong band ~ 753 cm^{-1} to ~ 757 cm^{-1} is imputed to the presence of di-Na-pentaborate and Li-pentaborate due to mixed alkali oxides present in the glassy network [57,58]. The shoulder band ~ 888 cm^{-1} to ~ 899 cm^{-1} is ascribed to the presence of a small amount of pyroborate units in BO_4 units. The rising band ~ 941 cm^{-1} to ~ 968 cm^{-1} and the shoulder band ~ 999 cm^{-1} to ~ 1018 cm^{-1} is attributed to increased orthoborate units with Li/Na-O-Fe vibrations [24,49,59,60]. The small emerging band ~ 1094 cm^{-1} to ~ 1111 cm^{-1} is imputed to different diborate groups [49,59]. The band ~ 1260 cm^{-1} to ~ 1307 cm^{-1} is assigned to existence of pyroborate groups in BO_3 units [30,49,58]. The emerging band ~ 1350 cm^{-1} to ~ 1367 cm^{-1} is attributed to BO_4^- linked to BO_2O^- triangles in the glass [30]. The shoulder bands ~ 1410 cm^{-1} to ~ 1445 cm^{-1} and ~ 1475 cm^{-1} to ~ 1511 cm^{-1} is ascribed to extension of B-O^- bonds or BO_2O^- triangles (NBOs) connected to an enormous borate group [49,59].

The presence of mixed-alkali oxides in the glass is higher with respect to the B_2O_3. This leads to the formation of pentaborate and di-pentaborate with the Li^+ and Na^+ ions, as displayed in **Figure 12**. This complex structure will occur only with a high concentration of alkali oxides (Li_2O and Na_2O) in the base glass coded BNLZF-00. As the concentration of Fe^{3+} increases, Fe_2O_3 partially replaces ZrO_2 and changes the glass network. The addition of Fe^{3+} ions disrupts the B-O-B bonds, leading to the creation of NBOs. The major formation of the orthoborate units is seen on behalf of

pentaborate and di-pentaborate groups, as shown in **Figure 13**. Since the formation of orthoborate leads to the formation of NBOs, some stretching vibration of BO_4 units with vibrations of Zr-O linkages were also observed in the network. This leads to the formation NBOs in the glassy network by the formation of an open structure, evidenced in the FTIR spectra.

Table 4: Band assignments of deconvoluted Raman spectra of BNLZF glasses.

BNLZF-00	BNLZF-02	BNLZF-04	BNLZF-06	BNLZF-08	BNLZF-10	Band assignments	Ref.
474	459	444	486	445	438	$[ZrO_4]$ unit's vibrations in Zr-O linkages.	[49,56,57]
522	503	495	564	488	481	Stretching of symmetrical bands of BO_4 units.	
754	756	757	754	754	753	Li-pentaborate and di-Na-pentaborate.	[57,58]
889	888	894	899	892	893	Pyroborate units in BO_4 units.	
941	946	964	968	965	965	Orthoborate units with Li/Na-O-Fe vibrations	[24,49,59,60]
1002	999	1013	1018	1013	1010		
1101	1111	1103	1104	1101	1094	Different diborate groups.	[49,59]

1307	1298	1301	1260	1268	1279	Pyroborate groups in BO_3 units.	[30,49,58]
1367	1366	1366	1356	1350	1365	BO_4^- linked to BO_2O^- triangles.	[30]
1445	1438	1444	1410	1414	1441	B-O^- bonds or BO_2O^- triangles (NBOs).	[49,59]
1511	1501	1497	1475	1486	1494		

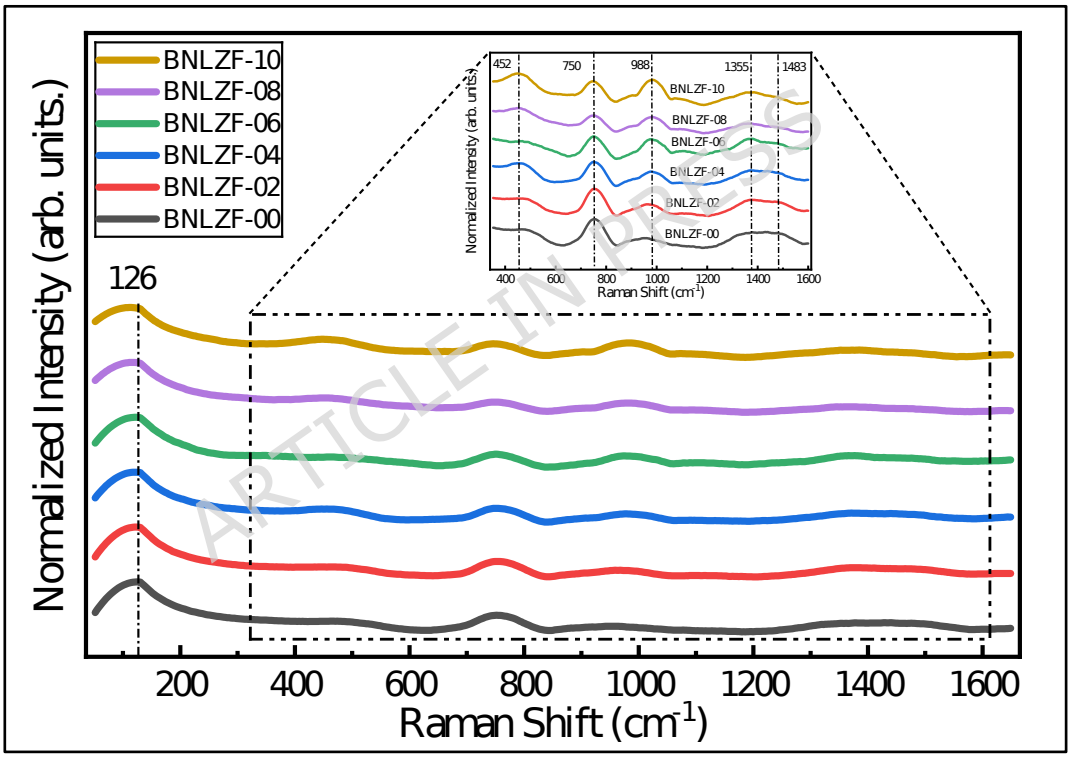

Figure 10: Raman spectra of BNLZF glasses.

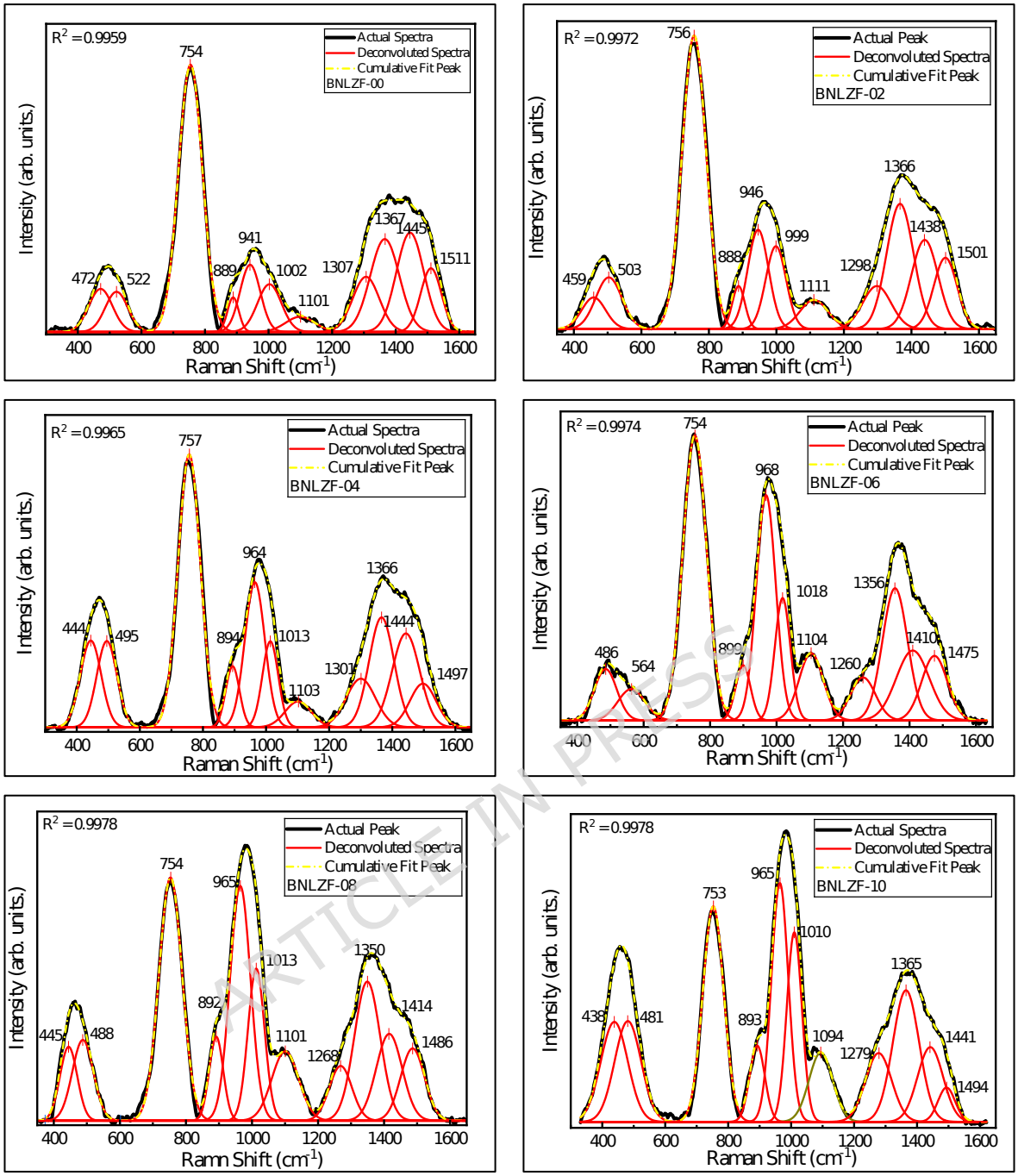

Figure 11: Deconvolution Raman spectra of BNLZF glasses.

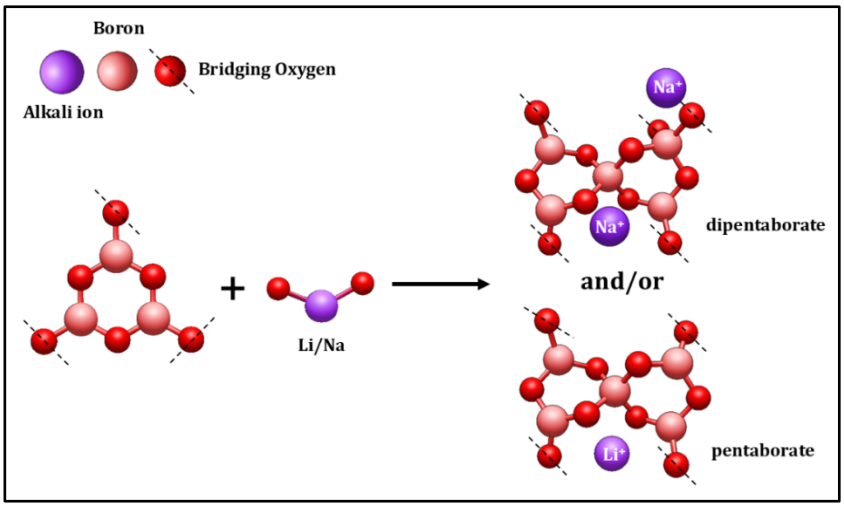

Figure 12: Formation of pentaborate and di-pentaborate in BNLZF-00 glass.

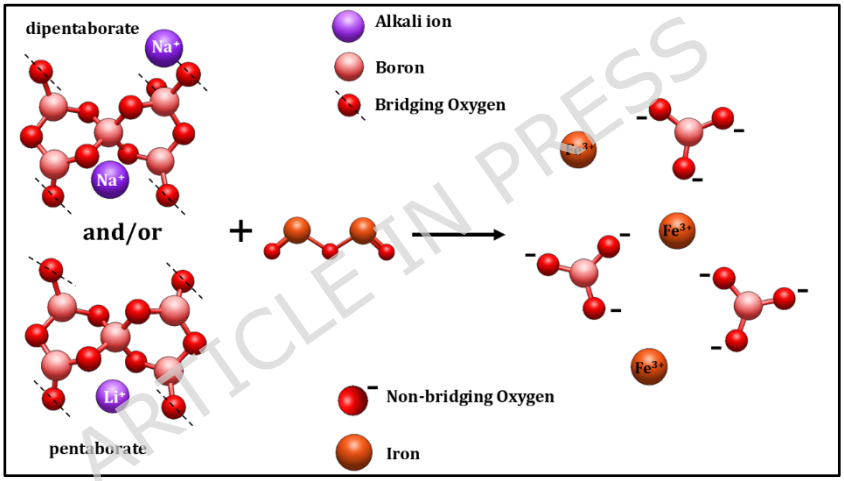

Figure 13: Formation of pentaborate and di-pentaborate to orthoborate in BNLZF-02 to BNLZF-10 glasses.

Optical Properties

Optical Absorption

Figure 14 illustrates the UV-Vis optical absorption spectra of the present BNLZF glasses. Additionally, it is noted that as Fe_2O_3 concentration increases, the absorption edge moves towards the longer wavelength, causing a redshift from 300 nm to 387 nm. This perceived redshift may be due to the transition of the electrons to the excited state from the valence band of the oxygen atom [61]. Among all the TMIs in the periodic table,

Fe^{3+}-ions, along with a d^5 configuration, are much scrutinised because they mostly exhibit weak prohibited transitions rather than a spin-allowed transition. The UV-Vis absorption band of the Fe^{3+} ions is observed to increase at ~ 450 nm with an increase in Fe_2O_3 concentration. This band is ascribed to $^6A_{1g}$ (^6S) → $^4A_{1g}$ (^4G); ^4E_g (^4G), a d-d transition of Fe^{3+} ions in the tetrahedral and/or distorted octahedral symmetrical structure in the network of the BNLZF glass [24,62]. The interaction of photons increases as the Fe^{3+} ion concentration is more in the glass matrix, with the reduction in the optical bandgap.

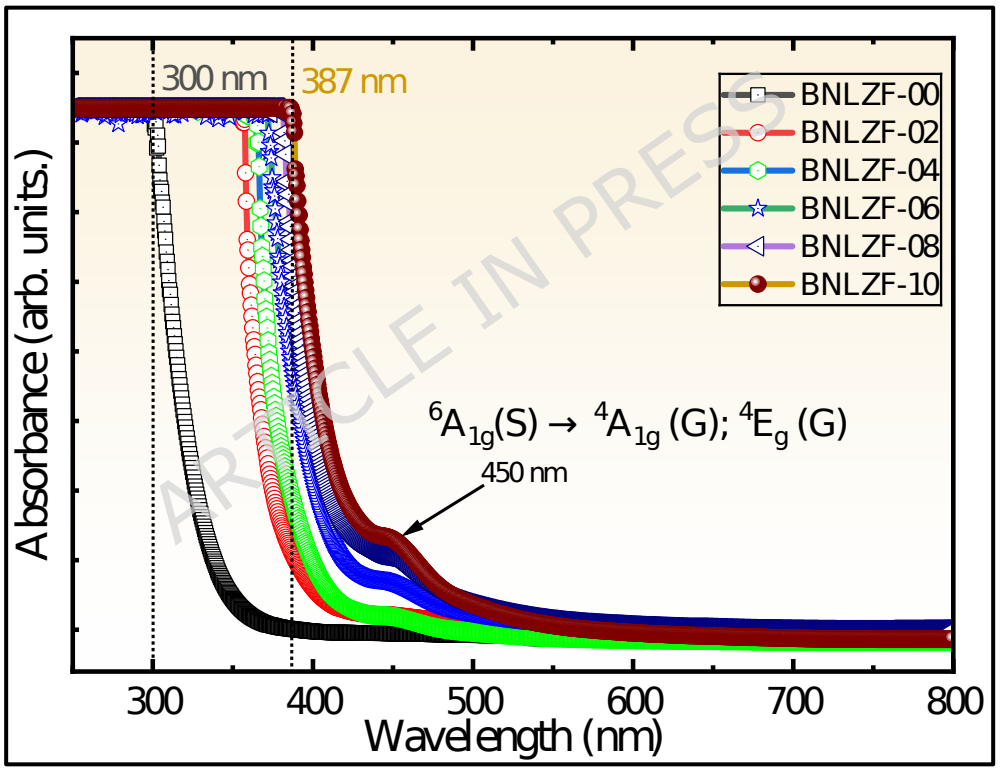

Figure 14: UV-Vis spectra of BNLZF glasses.

Optical bandgap (E_{opt})

Optical parameters are extracted from the optical absorption edge in the Tauc region (high-energy region) by absorption spectra. The Beer-Lambert law applies in amorphous glass systems because the samples are optically

uniform and free of scattering centres, allowing absorbance to be immediately transformed into the absorption coefficient. Therefore, the optical absorption coefficient, $\alpha(\nu)$ is evaluated by the following **equation 11**.

$$\alpha(\nu) = 2.303\ (A/d) \tag{11}$$

Where A and d are the absorbance in UV-Vis spectra and the glass sample thickness, respectively. This relationship is suitable for the current glass samples science light attenuation primarily results from intrinsic electronic absorption close to the band edge, ensuring accurate $\alpha(\nu)$ estimation for Tauc analysis. Further, the E_{opt} is calculated by the obtained optical absorption coefficient using Davis-Mott's expression given in **equation 12**.

$$\alpha h\nu = T(h\nu - E_{opt})^{i} \tag{12}$$

Where h is Planck's constant, $h\nu$ is the incident photon energy, T is the band tailing parameter. The values of the index i are chosen according to the selected electronic transition: direct allowed, direct forbidden, indirect allowed, and indirect forbidden, with the values 1/2, 3/2, 2, and 3, respectively [63,64]. The linear section of the obtained curve is extended as $(\alpha h\nu)^2$ tends to 0 and $(\alpha h\nu)^{1/2}$ tends to 0 on the x-axis in the plotted graph of direct bandgap and indirect bandgap values that are listed in **Table 5**. The direct bandgap $\left(E_{Opt}^{Dir}\right)$ reduced from 3.90 eV to 3.10 eV, and the indirect bandgap $\left(E_{Opt}^{Ind}\right)$ reduced from 3.44 eV to 2.77 eV, displayed in **Figures 15** and **16,** respectively. As a result, optical bandgap decreases, proving overall bandgap values are enhanced compared to those reported in previous investigations were listed in **Table 6**. The creation of NBOs due to an increase in the concentration of Fe_2O_3 leads to the reduction of the optical bandgap.

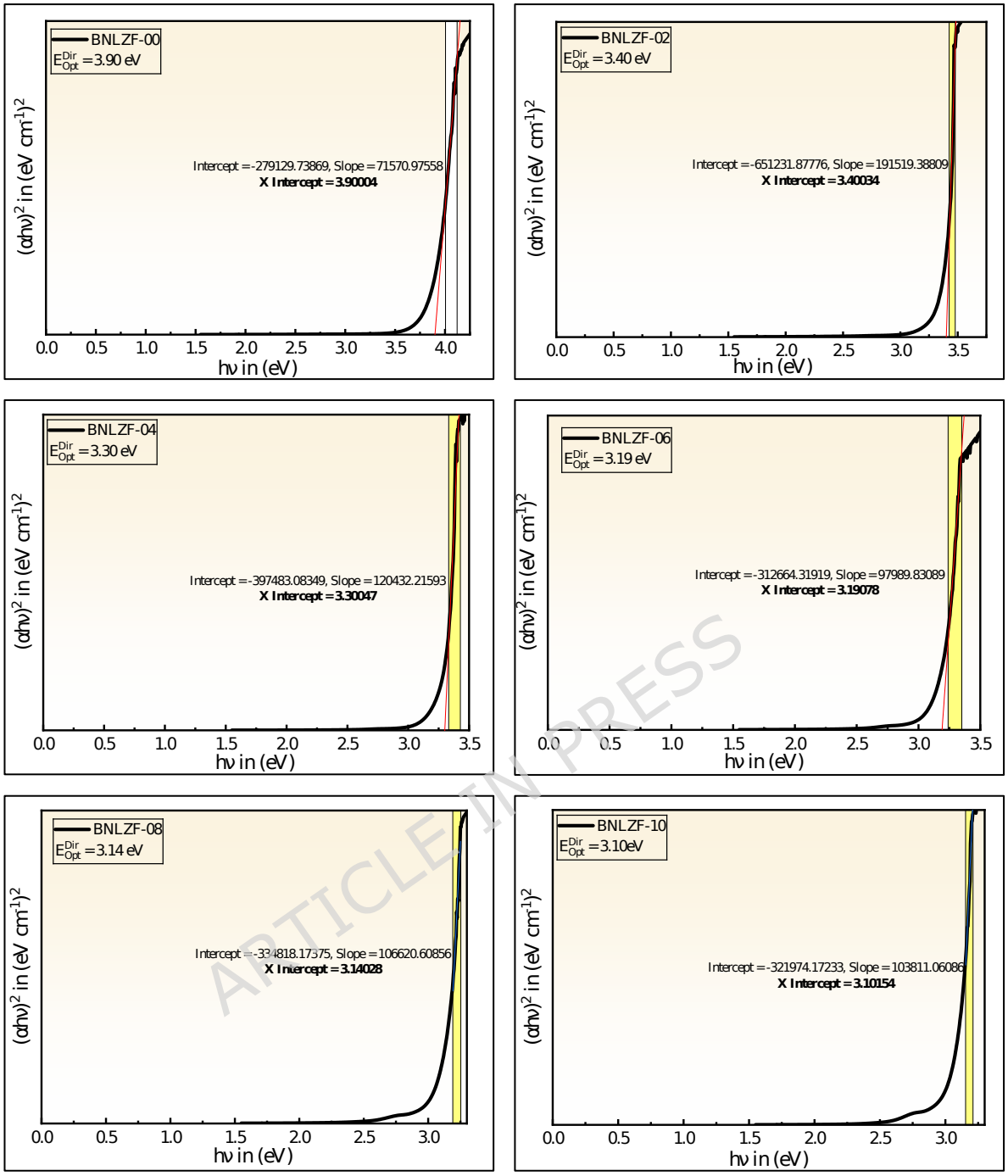

Figure 15: Direct bandgap of BNLZF glasses.

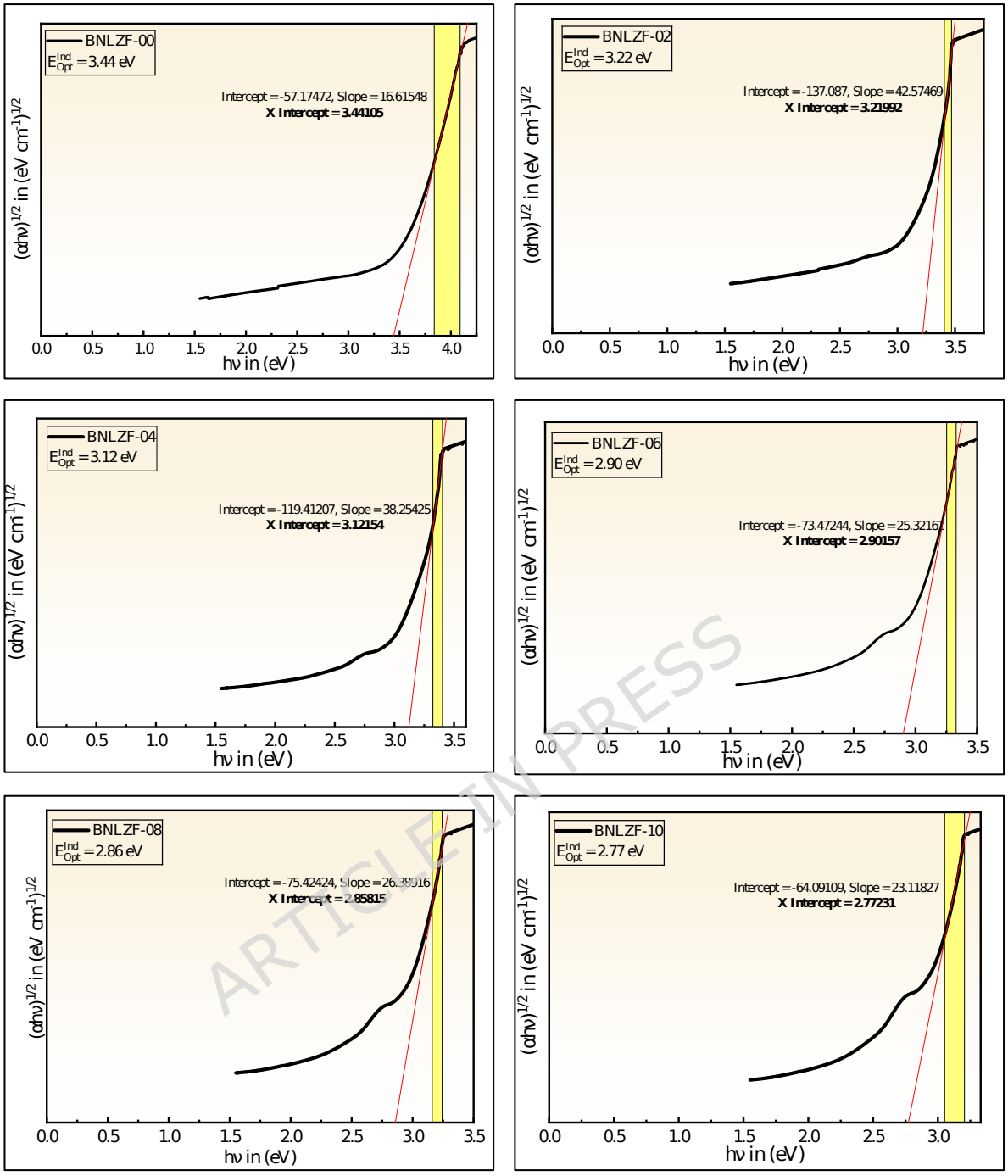

Figure 16: Indirect bandgap of BNLZF glasses.

Urbach Energy (U_E) and steepness parameter (σ_S)

The localized bandgap defect state, which blocks the electrons from transitioning directly from the valence band to the conduction band, is known as the Urbach energy. These localized bandgap defects cause the tail that is frequently seen in the optical absorption spectra and extends

into the forbidden bandgap. The Urbach energy (U_E) is measured by the width of the tail, which is related to the distortedness in the localized bandgaps. The following **equation 13** determines the U_E [64].

$$\alpha = \alpha_0 e^{h\nu/U_E} \tag{13}$$

The graph $\ln(\alpha)$ vs $h\nu$ (photon energy) is drawn to obtain the U_E, where α_0 is a constant. The U_E is calculated by obtaining the inverse of the slope as determined by **Figure 17** [65].

$$U_E = \frac{1}{\text{slope}} \tag{14}$$

The calculated U_E values are tabulated in **Table 5**. The values of U_E increased from 0.245 eV to 0.273 eV as the concentration of Fe_2O_3 is replaced with ZrO_2, compared with the bandgap in **Figure 18**. An increase in Fe^{3+} concentration creates localised states and NBOs in the glass network, leading to structural disorder. As a result, the optical bandgap decreases but the Urbach energy increases, indicating the degree of disorder in the glass matrix. The highest degree of disorderedness of obtained in BNLZF-10 glass. This explains the increase in disorderedness by Fe_2O_3, creating the open structure in the network of the glass by the formation of NBOs explained in FTIR and Raman spectroscopy.

The interactions of exciton-phonon and/or electron-phonon ($E_{(e\text{-}ph)}$) broaden the absorption edge, which is estimated from the steepness parameter σ_S, which is calculated by the following **equation 15 and 16** [65,66].

$$\sigma_S = k_B T/U_E \tag{15}$$

$$E_{(e\text{-}ph)} = 2/3\sigma_S \tag{16}$$

Where k_B and T are the Boltzmann constant and the room temperature (300 K), respectively. The computed data are listed in **Table 5**, and the decrease in values σ_S from 0.106 to 0.095, and the gradual increase in $E_{(e\text{-}ph)}$ from 6.302 to 7.039 due to the ionicity effect in glass and distinct anion charges in the current BNLZF glass, as shown in **Figure 18** [66].

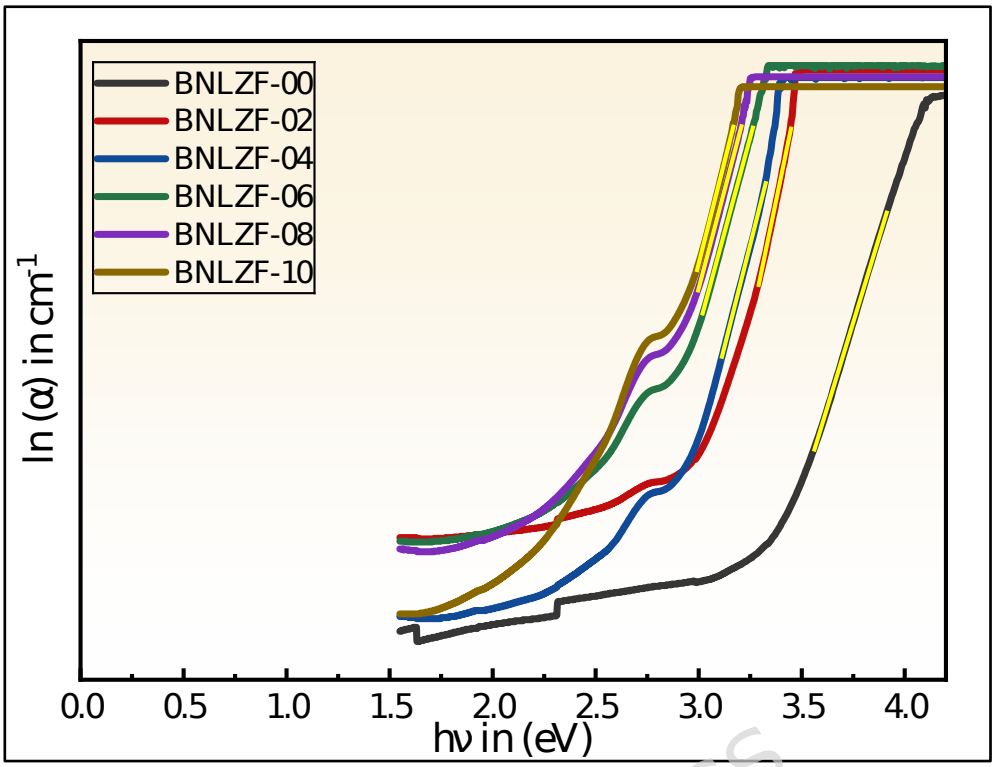

Figure 17: The Urbach energy of BNLZF glasses.

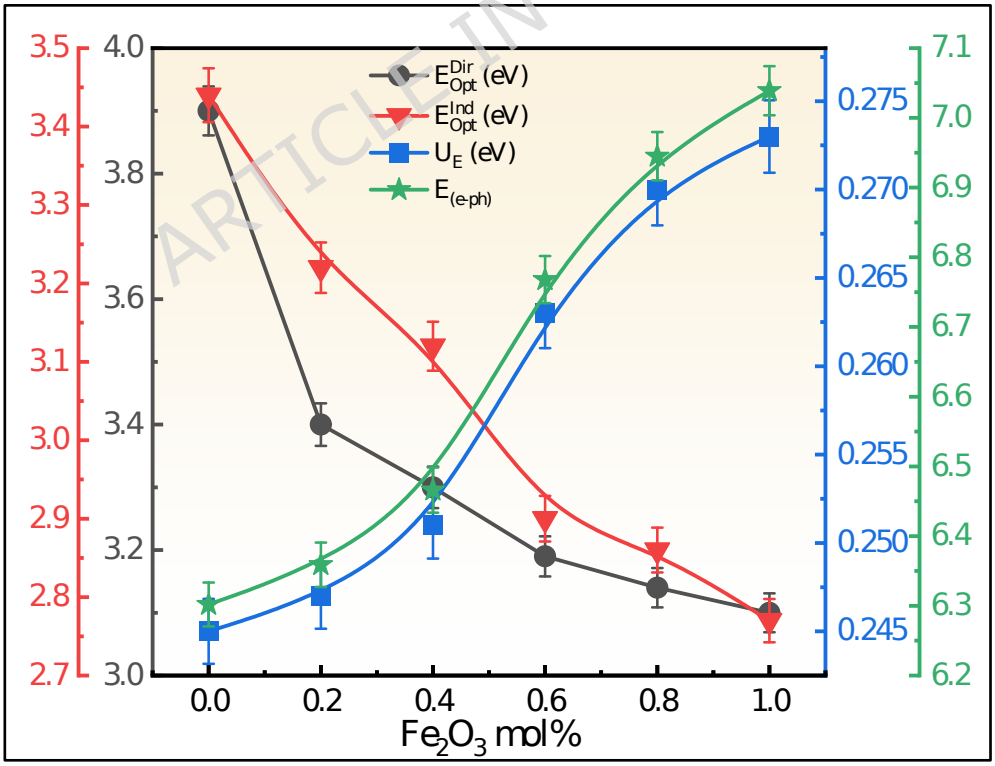

Figure 18: Comparison between E_{Opt}^{Dir}, E_{Opt}^{Ind}, U_E, and $E_{(e\text{-}ph)}$ of BNLZF glasses.

Dielectric constant (ε), optical dielectric constant (ε_{opt}), and linear dielectric susceptibility (χ_e)

The dipole orientation and refractive index contribute towards the polarizability of the glass, which contains a strong relationship with the values of ε, ε_{opt}, and χ_e, which is shown in the following relations:

$$\varepsilon = n^2 \tag{17}$$

$$\varepsilon_{opt} = n^2 - 1 \tag{18}$$

$$\chi_e = \frac{n^2 - 1}{4\pi} = \frac{\varepsilon_{opt}}{4\pi} \tag{19}$$

The calculated values are tabulated in **Table 5.** The measured values of the refractive index (n) varied from 1.54 to 1.57 and tabulated in **Table 5**. The ε values increased from 2.372 to 2.465, ε_{opt} values increased from 1.372 to 1.465, and χ_e values increased from 0.109 to 0.117, which confirms the linear dependency towards the values of n [54,65].

Reflection loss (R_L), transmittance coefficient (T_C) and numerical aperture (NA).

The following equations are utilized to calculate the reflection loss (R_L), transmittance coefficient (T_C), and numerical aperture (NA).

$$R_L = \left(\frac{n-1}{n+1}\right)^2 \times 100\% \tag{20}$$

$$T_C = \frac{2n}{n^2 + 1} \times 100\% \tag{21}$$

$$NA = n[2\Delta]^{1/2} \tag{22}$$

Where n is the refractive index and the Δ is the small change in RI (0.01). The R_L increased from 4.52 % to 4.92 % and T_C decreased from 91.35 % to 90.62 % due to adding Fe_2O_3 into the glass network. The value of NA ranging from 0.13 to 0.5 will be used as the core material in glass optical fibre cable. The NA of the present BNLZF glasses vary from 0.2178 to 0.222, and are compared in **Figure 19**, which is considered a promising

material for the core part of optical fiber cables [42,54,65,66]. The values are displayed in **Table 5**.

Molar refraction (R_m), molar electronic polarizability (α_m), and Metallization criterion (M)

The following **equations 23, 24, and 25** are obtained to compute the R_m, α_m, M to understand the molar polarizability and metallic nature of the BNLZF glass. The refractive index of the glass and the Lorentz-Lorentz equation are utilized to determine the metallic/non-metallic nature of the glasses based on R_m:V_m ratio as described by Dimitrov and Komatsu [67]. If R_m:V_m< 1, the material is non-metallic, and if R_m:V_m> 1, the material is metallic. Metallization criterion of the BNLZF glasses is calculated in accordance with the Herzfeld theory of metallization [38,42,64–66].

$$R_m = \left[\frac{n^2-1}{n^2+2}\right]V_m \tag{23}$$

$$\alpha_m = \frac{R_m}{2.52} \tag{24}$$

$$M = \frac{R_m}{V_m} \tag{25}$$

Where n is the refractive index and V_m is the molar volume of the BNLZF glass, and calculated values are tabulated in **Table 5**, and compared in **Figure 19**. R_m increased to 16.16 cm^3 from 15.01 cm^3 and α_m increased to 6.41 $Å^3$ from 5.96 $Å^3$ as the Fe^{3+} ions were introduced into the glass network. Whereas M values reduced to 0.672 from 0.686. Additionally, materials with a high cap M value, close to 1, are considered insulators, and those with a low cap M value, close to 0, are considered metals [54,65]. In BNLZF glass influence of Fe^{3+} on the glass leads to enhancing the metallic nature of the glass.

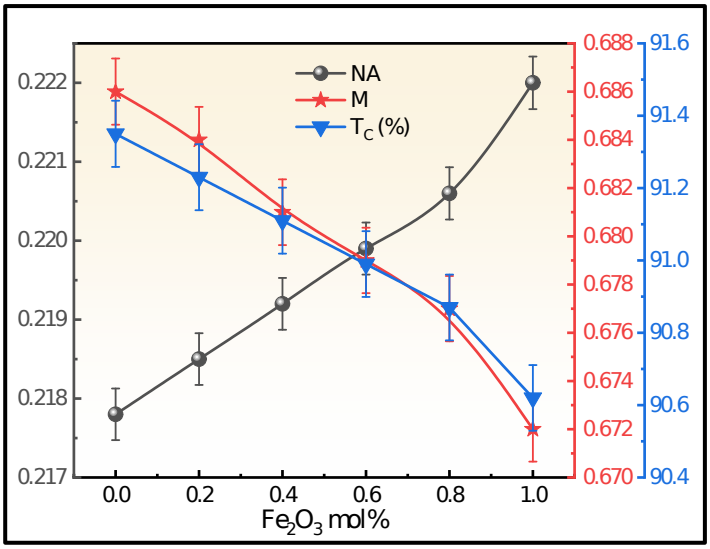

Figure 19: Comparison of NA, M, and T_C of BNLZF glass samples.

Electronegativity (χ), electron polarizability (α_0)

The following **equation 26** is used to calculate electronegativity (χ) which has the ability of an atom to attract the shared electrons to be involved in a chemical bond in the network of the glass, and **equation 27** is used to calculate electron polarizability (α_0) which describes the effect of the external electric field to distort the electron clouds present in the glass structure [66,68].

$$\chi = 0.2688\ E_{Opt}^{Ind} \quad (26)$$

$$\alpha_0 = -0.9(\chi) + 3.5 \quad (27)$$

χ show a reduction in the values from 0.925 to 0.745. A rise in the α_0 values from 2.668 to 2.830 are seen in the BNLZF glasses. These obtained values explain the ionic nature and formation of NBOs in the BNLZF glasses due to the increase in Fe^{3+} concentration. The computed data were listed in **Table 5**.

Electronic oxide ion polarizability ($\alpha_{O^{2-}}$)

The electronic oxide polarizability ($\alpha_{O^{2-}}$) measures the distortion of the electron clouds of oxide ions (O^{2-}), which is affected by the external electric

field. The equation given below is used to determine $\alpha_{O^{2-}}$ by refractive index (n) and optical bandgap (E_{Opt}^{Ind}) [38,42,54,65].

$$\alpha_{O^{2-}}(n) = \left[\left(\frac{R_m}{2.52}\right) - \sum \alpha_c\right] \Big/ \left[N^{O^{2-}}\right] \quad (28)$$

$$\alpha_{O^{2-}}(E_{Opt}^{Ind}) = \left[\left(\frac{V_m}{2.52}\right)\left(1 - \sqrt{\frac{E_{Opt}^{Ind}}{20}}\right) - \sum \alpha_c\right] \Big/ \left[N^{O^{2-}}\right] \quad (29)$$

Where $\sum \alpha_c$ is molar cation polarizability, which is given by $v\times2\times\alpha_{B^{3+}} + w\times2\times\alpha_{Na^{+}} + x\times2\times\alpha_{Li^{+}} + y\times1\times\alpha_{Zr^{4+}} + z\times2\times\alpha_{Fe^{3+}}$ from the stoichiometry ratio $vB_2O_3 – wNa_2O – xLi_2O – yZrO_2 – zFe_2O_3$. The values of $\alpha_{B^{3+}}$ = 0.002 Å^3, $\alpha_{Na^{+}}$ = 0.181 Å^3, $\alpha_{Li^{+}}$ = 0.029 Å^3, $\alpha_{Zr^{4+}}$ = 0.377 Å^3, $\alpha_{Fe^{3+}}$ = 0.437 Å^3 and $N^{O^{2-}}$ is the number of oxide ions in the glass matrix $v\times3+w\times1+x\times1+y\times2+z\times3$. The calculated electronic oxide polarizability using the optical bandgap $\left(\alpha_{O^{2-}}(E_{Opt}^{Ind})\right)$ and refractive index ($\alpha_{O^{2-}}(n)$) is increased from 4.780 to 5.258 [69,70], and from 2.538 to 2.722, respectively. These obtained values are noted in **Table 5**, and enhanced values are displayed in **Table 6**. It shows an increasing trend with refractive index and optical bandgap, which is attributed to the formation of NBOs, creating an open structure allowing more distortion in the electron clouds of the oxide ions in the glass network. The comparison of the values is illustrated in **Figure 20**.

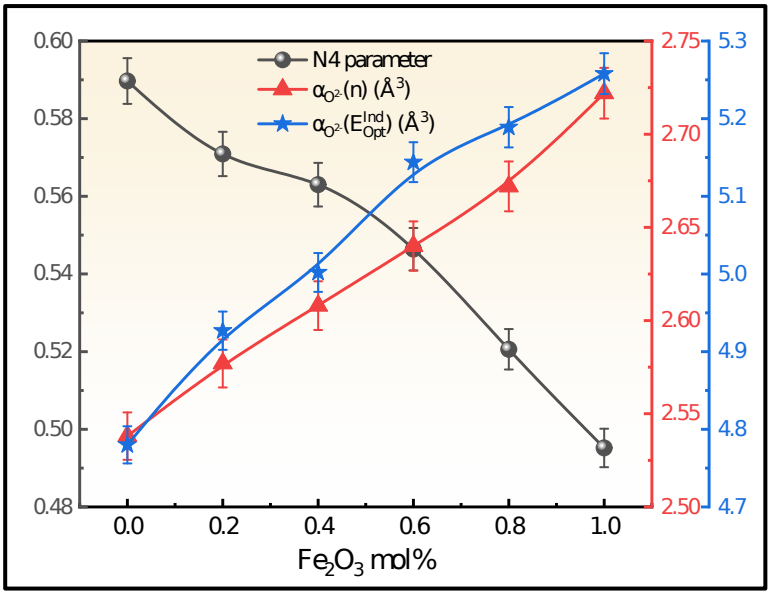

Figure 20: Comparison of N4, ($\alpha_{O^{2-}}(n)$), and $\left(\alpha_{O^{2-}}(E_{Opt}^{Ind})\right)$ of BNLZF glass samples.

Optical basicity (Λ)

Optical basicity (Λ) is the quantitative measurement of oxide (II) atoms in electron-donor strength in oxidic networks. The following **equations 30, 31,** and **32** are used to calculate the Λ by electronegativity (χ), electronic ion polarizability with refractive index (n), and optical bandgap (E_{Opt}^{Ind}) respectively [42,64,66].

$$\Lambda_{\chi} = -0.5\chi + 1.7 \tag{30}$$

$$\Lambda_{n} = 1.67\left(1 - \frac{1}{\alpha_{O^{2-}}(n)}\right) \tag{31}$$

$$\Lambda_{E_{Opt}^{Ind}} = 1.67\left(1 - \frac{1}{\alpha_{O^{2-}}(E_{Opt}^{Ind})}\right) \tag{32}$$

The optical basicity of the BNLZF glasses was calculated and exemplified in **Table 5**. Λ_{χ},$\Lambda_{E_{Opt}^{Ind}}$, and Λ_{n} values are increased from 1.238 to 1.328, from 1.321 to 1.352 [69,70], and from 1.012 to 1.056 as the Fe_2O_3 is replaced with ZrO_2 and the compared values are illustrated in **Table 6**. The extra oxygen atom from Fe_2O_3 replacing ZrO_2 enhances the optical

basicity in the glass system as the oxygen concentration increases in the glass network [71]. The comparison of these values with E_{Opt}^{Ind} is displayed in **Figure 21.**

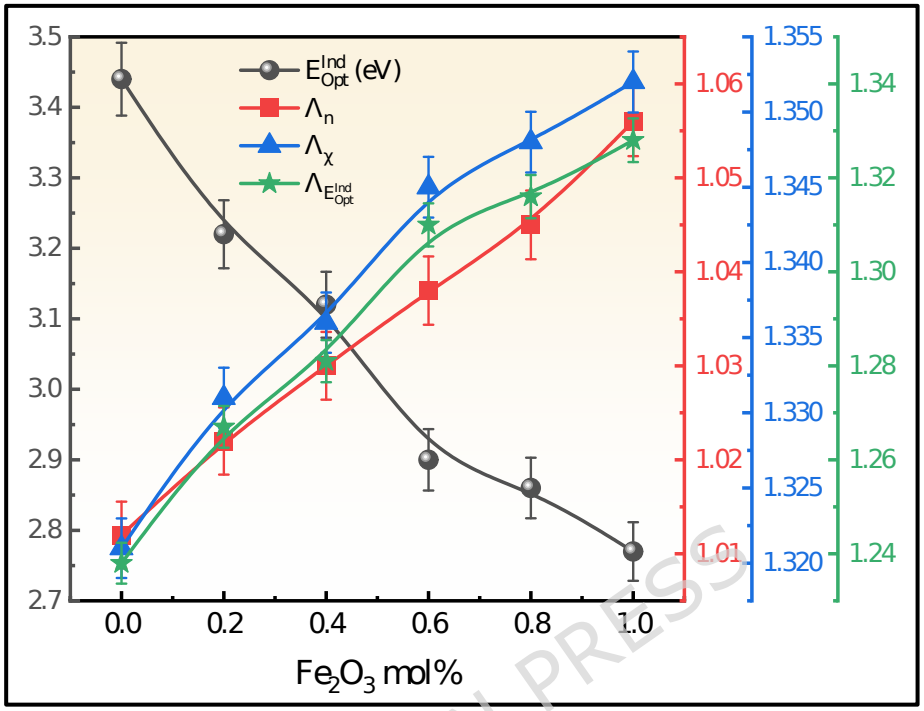

Figure 21: Comparison of optical basicity with E_{Opt}^{Ind} of BNLZF glasses.

Third-order susceptibility ($\chi^{(3)}$), and non-linear refractive index (n_2)

Third-order susceptibility is directly related to the nonlinear optical (NLO) refractive index, which is the intensity-dependent change in the refractive index of materials. When high-intensity electromagnetic waves interact with dielectric materials, their nonlinear characteristics emerge, making third-order behaviour significant. $\chi^{(3)}$ and n_2 Using Ticha-Tichy **equations 33** and **34,** given below [72]:

$$\chi^{(3)} = A\left[\frac{n^2-1}{4\pi}\right]^4 \quad (33)$$

$$n_2 = \frac{12\pi\chi^{(3)}}{n} \quad (34)$$

Where A (1.7×10^{-10} esu) is the constant. The computed data are tabulated in **Table 5**. The addition of Fe_2O_3 to the composition has shown increasing

n_2 values increase from 5.90 × 10^{-13} esu to 7.54 × 10^{-13} esu and $\chi^{(3)}$ values increase from 2.41 × 10^{-14} esu to 3.14 × 10^{-14} esu [73]. These n_2 and $\chi^{(3)}$ values are enhanced compared to recent literature in **Table 6**. Linear and nonlinear susceptibility and refractive index show an increasing trend and are displayed in **Figure 22**. As the concentration of Fe^{3+} increases, the refractive index of the glass increases due to increased electronic polarizability and localised electronic states. An increase in the refractive index values promotes the interaction between the electromagnetic field and the glass network, leading to an increase in the n_2 and $\chi^{(3)}$ values. This makes the current BNLZF glasses suitable for a wide range of applications in nonlinear optical instruments, optical switching, and advanced communication technology [74].

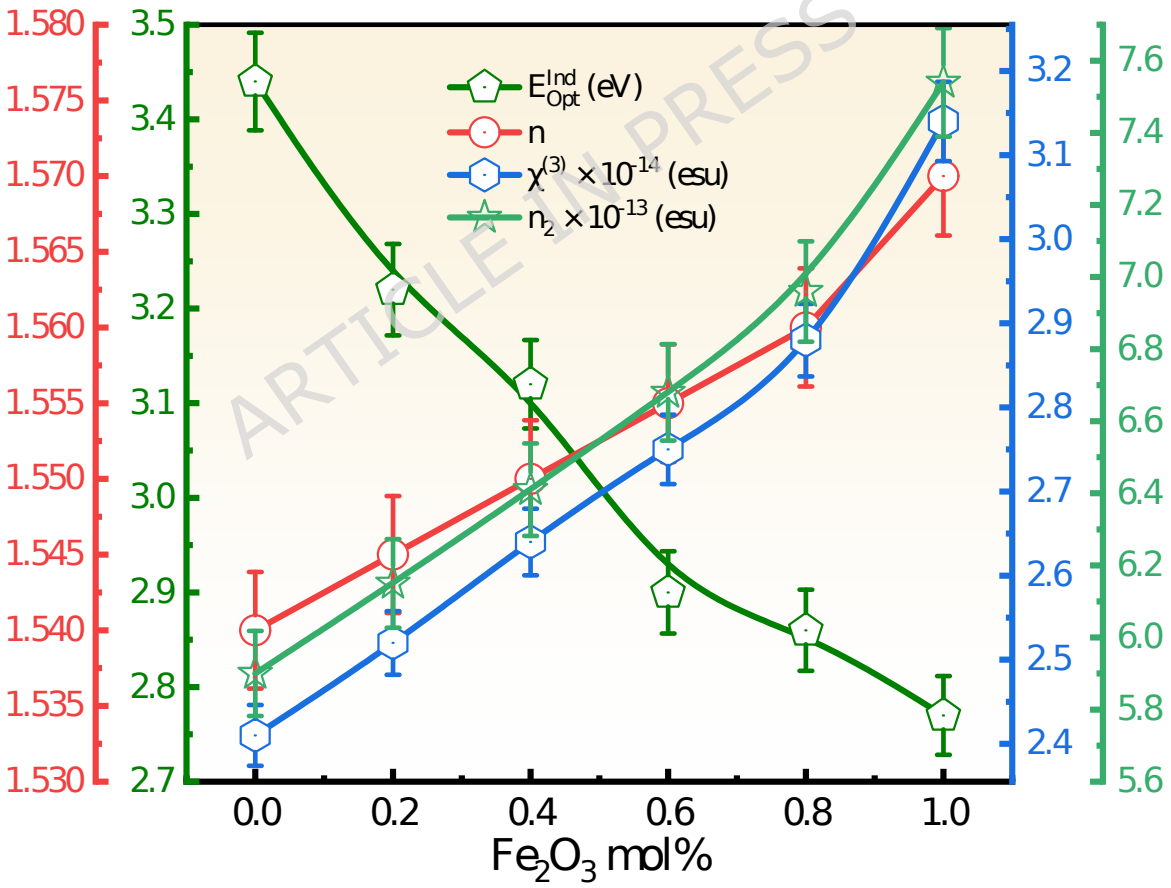

Figure 22: Comparison of E_{Opt}^{Ind} with n, n_2 and $\chi^{(3)}$ of BNLZF glasses.

Table 5: Optical parameters of the BNLZF glasses with error range ±0.001.

Sample Code	**BNLZF -00**	**BNLZF -02**	**BNLZF -04**	**BNLZF -06**	**BNLZF -08**	**BNLZF -10**
E_{Opt}^{Dir} (eV)	3.90	3.40	3.30	3.19	3.14	3.10
E_{Opt}^{Ind} (eV)	3.44	3.22	3.12	2.90	2.86	2.77
U_E (eV)	0.245	0.247	0.251	0.263	0.270	0.273
σ_S	0.106	0.105	0.103	0.098	0.096	0.095
$E_{(e\text{-}ph)}$	6.302	6.359	6.466	6.768	6.945	7.039
n	1.54	1.55	1.55	1.56	1.56	1.57
ε	2.372	2.387	2.403	2.418	2.434	2.465
ε_{opt}	1.372	1.387	1.403	1.418	1.434	1.465
χ_e	0.109	0.110	0.112	0.113	0.114	0.117
R_L	4.52	4.59	4.65	4.72	4.79	4.92
T_C	91.35	91.23	91.11	90.99	90.87	90.62
NA	0.2178	0.2185	0.2192	0.2199	0.2206	0.2220
R_m (cm^3)	15.01	15.25	15.45	15.65	15.85	16.16
α_m ($Å^3$)	5.96	6.05	6.13	6.21	6.29	6.41
M	0.686	0.684	0.681	0.679	0.677	0.672
χ	0.925	0.866	0.839	0.780	0.769	0.745
α_0	2.668	2.721	2.745	2.798	2.808	2.830
$\alpha_{O^{2-}}(n)$ ($Å^3$)	2.538	2.577	2.608	2.640	2.672	2.722
$\alpha_{O^{2-}}\left(E_{Opt}^{Ind}\right)$ ($Å^3$)	4.780	4.927	5.002	5.144	5.189	5.258
Λ_χ	1.238	1.267	1.281	1.310	1.316	1.328
Λ_n	1.012	1.022	1.030	1.038	1.045	1.056
$\Lambda_{E_{Opt}^{Ind}}$	1.321	1.331	1.336	1.345	1.348	1.352
$n_2 \times 10^{-13}$ (esu)	5.90	6.15	6.41	6.68	6.96	7.54
$\chi^{(3)} \times 10^{-14}$ (esu)	2.41	2.52	2.64	2.75	2.88	3.14

Table 6: Compared optical parameters with BNLZF glass.

Glass Matrix	**Optical band gap, eV**	**Electronic oxide ion polarizability, Å³**	**Optical basicity**	**Third-order susceptibility, × 10^{-14} (esu)**	**Non-linear refractive index, × 10^{-13} (esu)**	**Ref**
$60B_2O_3$ - $25Na_2O$ - $10Li_2O$ - $4ZrO_2$ - $1Fe_2O_3$	2.77	5.258	1.352	3.14	7.54	Present Work
$35Bi_2O_3$ – $40B_2O_3$ – $24TeO_2$ – $1Fe_2O_3$	2.7601	3.5807	1.2036			[70]
$35P_2O_5$ – $40ZnO$ – $25Na_2O$ – $1Fe_2O_3$	2.869	-	-	-	-	[75]
$59P_2O_5$ – $37PbO_2$ – $3As_2O_3$ – $1Fe_2O_3$	2.78	-	0.764	0.3327	0.5043	[76]
$65B_2O_3$ – 15NaF – 15ZnO – $5Bi_2O_3$ – $0.5Fe_2O_3$ – 0CuO	3.595	-	-	-	-	[77]

$10SiO_2$ – $65B_2O_3$ – $24Na_2O$ – $1Fe_2O_3$	2.97	-	1.04	3.58	5.61	[78]

Photoluminescence (PL) Spectra

Figures 23 & 24 show the excitation (λ_{exi}) spectra and emission (λ_{emi}) spectra of Fe^{3+} doped mixed alkali zirconia borate glasses. The PL spectra of BNLZF glasses arise due to the d^5 configuration, which exhibits spin-forbidden d-d electronic transitions. The peaks in the excitation spectra, obtained at (i) 424 nm is due to the $^6A_1(^6S) \rightarrow {}^4T_2(^4D)$, (ii) 486 nm is due to the $^6A_1(^6S) \rightarrow {}^4E,{}^4A_1(^4G)$, and (iii) 550 nm, 560 nm and 570 nm is due to the $^6A_{1g}(^6S) \rightarrow {}^4T_{2g}(^4G)$ transition [79,80]. The excitation is fixed at 550 nm, 560 nm and 570 nm, and the emission of a broad peak is observed at 598 nm is ascribed to the $^4T_{2g}(^4G) \rightarrow {}^6A_{1g}(^6S)$ and the shoulder peak at 650 nm is assigned to the $^4T_{1g}(^4G) \rightarrow {}^6A_{1g}(^6S)$ transition [80]. The intensity of the emission spectra increases as the Fe^{3+} concentration is increased in the BNLZF glass system by maintaining the orange-red emission at 598 nm. The increase in PL intensity is due to more Fe^{3+} ions absorbing photons at the excitation wavelength, creating a larger population of excited Fe^{3+} centres. Furthermore, the glasses do not exhibit concentration quenching within the investigated matrix range, suggesting the non-radiative mechanisms, like energy migration to quenching sites/cross-relaxation, are still confined. Therefore, both the preservation of an efficient radiative transition and the increasing number of Fe^{3+} centres are responsible for the increase in PL intensity. The schematic representation of the energy level diagram of the PL spectra is shown in **Figure 25**. The orange-red colour emission at 598 nm leads to a prominent material for photonics applications.

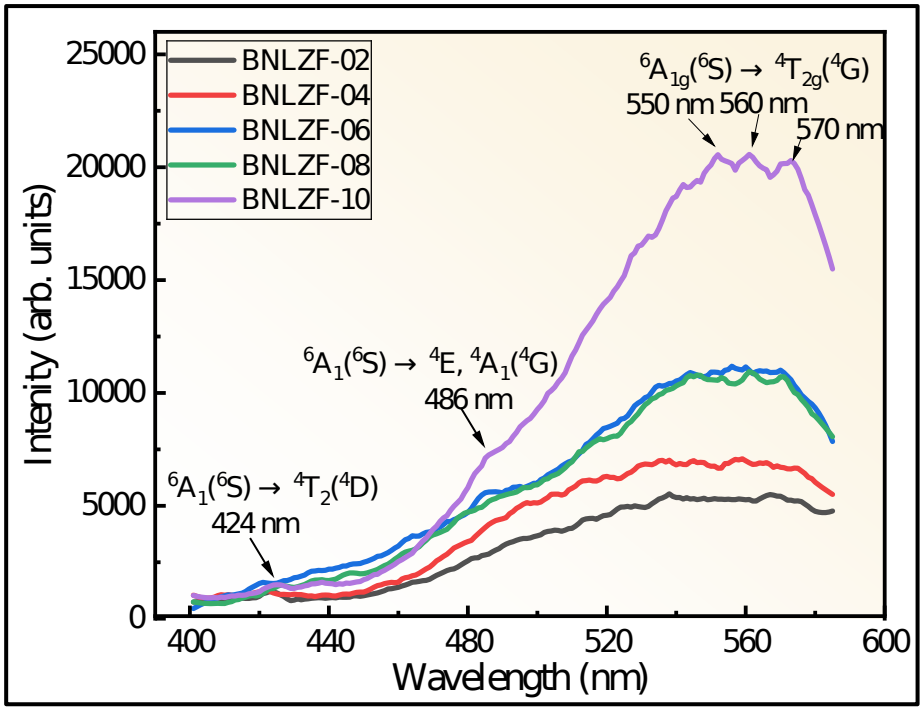

Figure 23: The excitation spectra (λ_{emi} = 598 nm) of BNLZF glass.

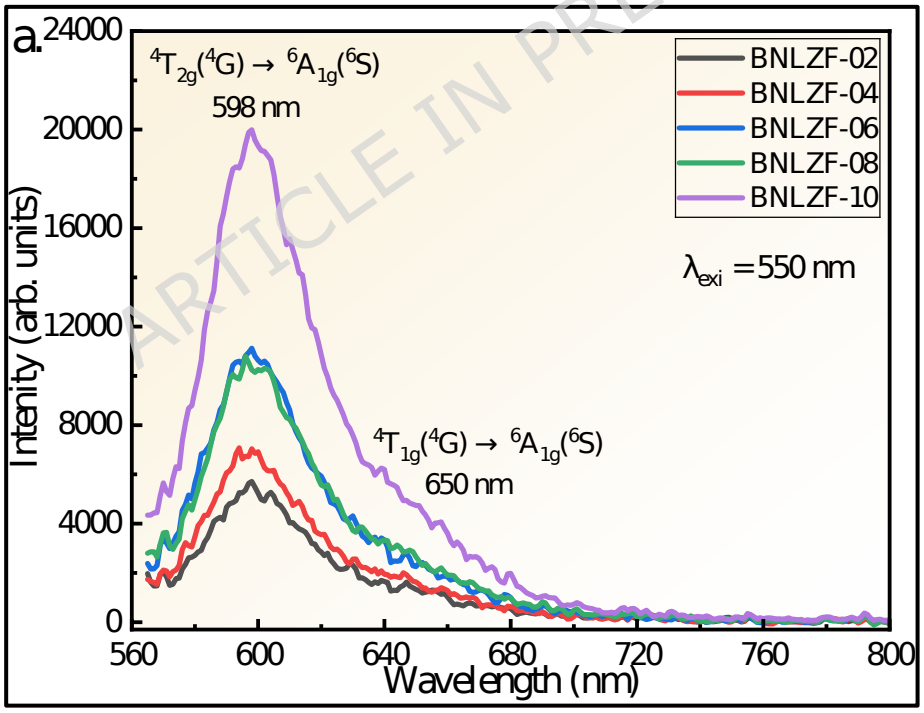

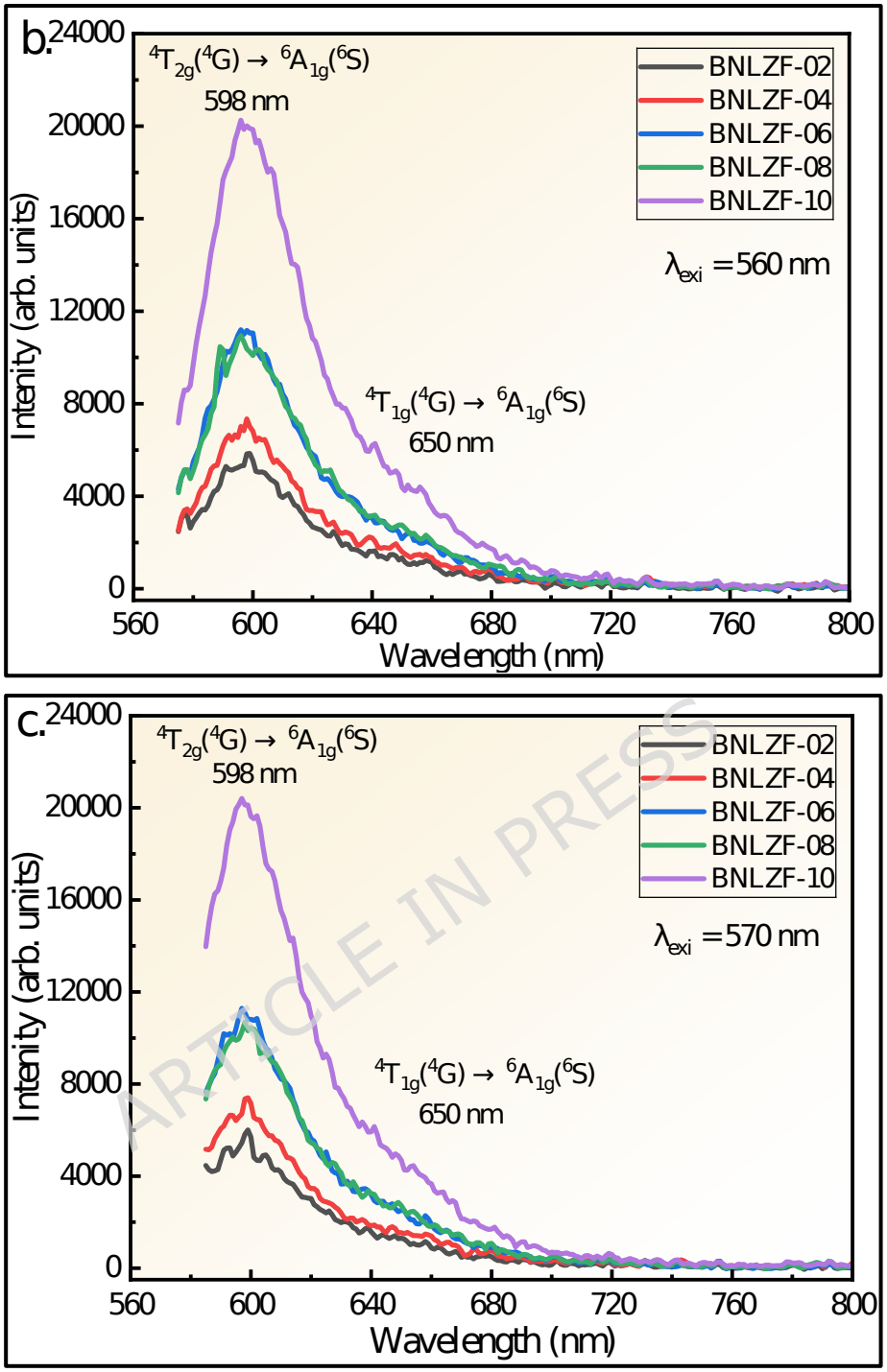

Figure 24: Emission spectra **a.** λ_{exi} at 550 nm **b.** λ_{exi} at 560 nm and **c.** λ_{exi} at 570 nm of BNLZF glass.

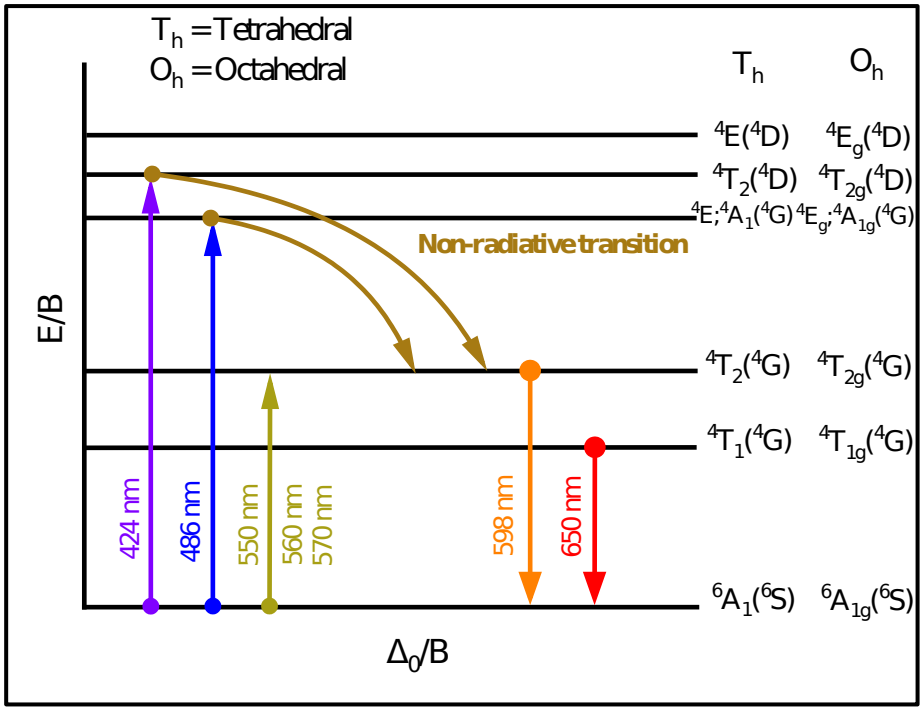

Figure 25: Schematic representation of the d^5 energy level diagram.

The Commission Internationale de l'Éclairage (CIE) chromaticity diagram was utilised to assess the coordinates of the chromaticity of BNLZF glasses. The coordinates for synthesized BNLZF glasses are shown in **Table 6**, and they fall within the orange-red zone of the CIE diagram, as seen in **Figure 26**. The CIE coordinates of BNLZF glasses meticulously resemble the coordinates (0.536, 0.444) of the renowned orange-red phosphor [81]. In accordance with this correlation, BNLZF glasses doped with Fe^{3+} exhibit pledge for orange-red photonic applications.

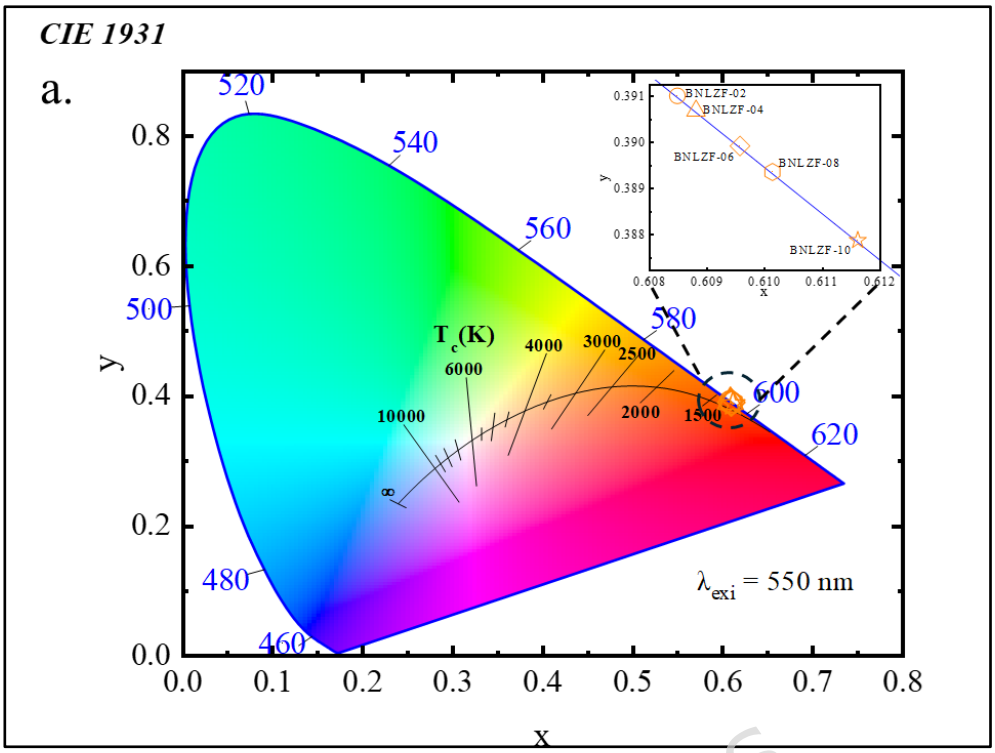

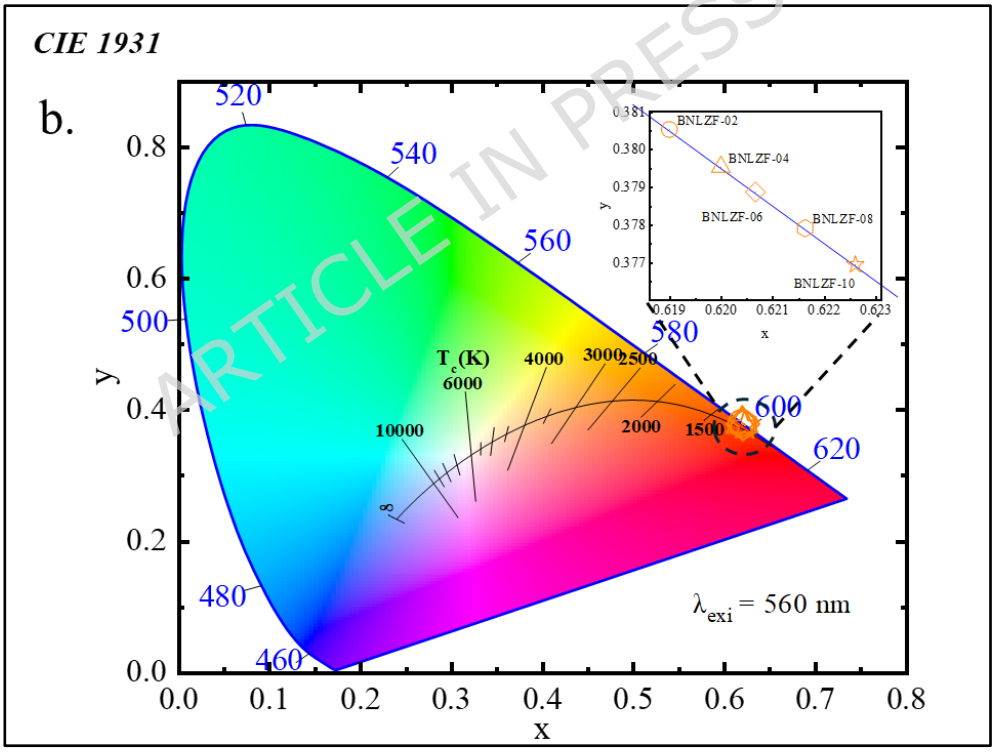

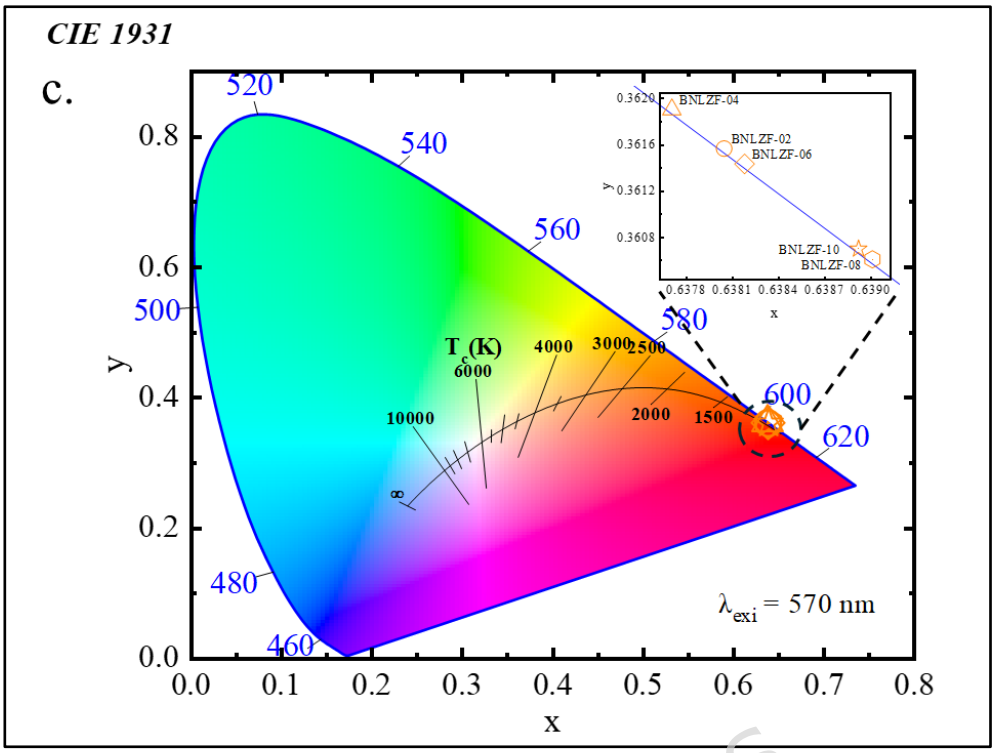

Figure 26: The CIE chromaticity diagram **a.** λ_{exi} at 550 nm **b.** λ_{exi} at 560 nm and **c.** λ_{exi} at 570 nm of BNLZF glass.

Additionally, the temperature of a Planckian blackbody radiator generating a colour most comparable to the observed source at the same brightness level was computed, which is known as the Correlated Colour Temperature (CCT). The CCT values were calculated using McCamy's empirical formula [82,83]:

$$CCT = -449m^3 + 3525m^2 - 6823.3m + 5520.33 \quad (35)$$

Where (x, y) are the coordinates determined from the CIE chromaticity diagram of the synthesized BNLZF glasses, $m = (x-x_a)/(y-y_a)$ is the inverse slope line, and x_a and y_a are the epicentres with the values of 0.332 and 0.186, respectively. The values of CCT for the prepared glass samples are listed in **Table 7**.

At the λ_{exi} = 550 nm, the CCT values increased linearly from 1628 K to 1639 K with the gradual increase in the Fe^{3+} concentration, showing a stable orange-red emission region. At λ_{exi} = 560 nm, CCT values increased from 1684 K to 1718 K, indicating a steady shift in chromaticity

coordinates to the reddish region. Conversely, at λ_{exi} = 570 nm, the CCT values fluctuated between 1972 K to 1980K, exhibiting a slightly non-linear dependence on Fe^{3+} concentration. This variation is attributed to changes in the Fe^{3+} site symmetry within the glass matrix in addition to local field effects in the glass network. These Fe^{3+} doped glasses exhibit low CCT values (below 2000 K) and emit warm light, making them suitable for laser active materials, optical amplifiers, and warm photonic applications [81,84].

Table 7: The CIE coordinates and the CCT values of BNLZF glasses with error range ±0.001.

Sample Code	λ_{exi} **(nm)**	**CIE coordinates**		m	**CCT (K)**
		x	y		
BNLZF-02	550	0.6085	0.3910	1.3486	1628
BNLZF-04		0.6088	0.3907	1.3523	1629
BNLZF-06		0.6096	0.3899	1.3611	1631
BNLZF-08		0.6101	0.3894	1.3676	1633
BNLZF-10		0.6116	0.3879	1.3848	1639
BNLZF-02	560	0.6190	0.3805	1.4754	1684
BNLZF-04		0.6200	0.3795	1.4881	1693
BNLZF-06		0.6207	0.3789	1.4966	1699
BNLZF-08		0.6216	0.3779	1.5091	1708
BNLZF-10		0.6226	0.3770	1.5219	1718
BNLZF-02	570	0.6381	0.3616	1.7432	1959
BNLZF-04		0.6377	0.3619	1.7379	1952
BNLZF-06		0.6382	0.3614	1.7452	1962
BNLZF-08		0.6390	0.3606	1.7583	1980
BNLZF-10		0.6389	0.3607	1.7568	1978

Conclusion

The study on the BNLZF glass series was synthesised through the melt quenching technique.

i. XRD confirms the non-crystallinity by X-ray diffraction. Morphological and elemental analysis studies were seen through SEM images and EDS spectra, respectively.

ii. The ρ values were increased from 2.4197 $g.cm^{-1}$ to 2.4324 $g.cm^{-1}$, and V_m values increased from 47.8548 $cm^3.mol^{-1}$ to 49.2567 $cm^3.mol^{-1}$. Furthermore, the physical properties followed the same trend corresponding to the ρ and V_m values.

iii. Deconvolution of the FTIR and Raman spectra explained the conversion of pentaborate and di-pentaborate to orthoborate units, verified with the decrease in N4 parameter value to 0.4952 from 0.5837 as the NBOs increased in the glass network.

iv. The optical absorption band was observed at 450 nm, corresponding to the d-d electronic transition $^6A_{1g}$ (^6S) → $^4A_{1g}$ (^4G); ^4E_g (^4G). The redshift was observed from 300 nm to 387 nm as the concentration of Fe_2O_3 increased in BNLZF glass.

v. The direct optical bandgap decreased from 3.93 eV to 3.10 eV, and the indirect optical bandgap decreased from 3.44 eV to 2.77 eV. The Urbach energy increased from 0.245 eV to 0.273 eV, confirming the distortion in the glass system.

vi. The n values were increased from 1.54 to 1.57. The optical parameters were evaluated using the n and the optical bandgap. The n_2 and $\chi^{(3)}$ values are found to be increased, and the values showed that BNLZF glasses were potentially suitable for nonlinear optical applications.

vii. The PL spectra display orange-red emission centred at 598 nm attributed to the $^4T_{2g}(^4G) \rightarrow {}^6A_{1g}(^6S)$ transition, with a shoulder peak at 650nm from the $^4T_{1g}(^4G) \rightarrow {}^6A_{1g}(^6S)$ transition. The excitation bands confirm efficient visible absorption from Fe^{3+} ions in mixed coordination sites. Increasing Fe^{3+} concentration enhances emission intensity while maintaining colour stability within the orangish-red region (CCT < 2000 K).

Overall, the findings show a strong relationship between structural modification and ensuring optical and luminescence properties, bridging the research gap and suggesting that the BNLZF glasses are promising materials for warm orange-red photonic applications.

Acknowledgments

The authors would like to thank and acknowledge Manipal Institute of Technology Bengaluru, and Manipal Academy of Higher Education, Manipal, for their great encouragement and support towards research. The authors express thanks to the Centre for Nano and Soft Matter Sciences (CeNS), Bengaluru, for providing Raman Spectroscopy characterizations and Jawaharlal Nehru Centre for Advanced Scientific Research (JNCASR), Bengaluru, for their support with Powder XRD measurements.

Authors contributions

Vinay D: Conceptualisation, Data curation, Investigation, Formal analysis, Writing – original draft.

C Devaraja: Conceptualization, Data curation, Methodology, Writing – review & editing, Validation, Supervision.

Utpal Deka: Writing – review & editing, Validation, Supervision.

R.S. Gedam: Validation, Methodology, Data curation.

Declarations

Competing interests

The authors declare no competing interests.

Data availability

The data used and/or analysed during the current study are available from the corresponding author on reasonable request.

Funding:

The author received **No Funding** for this work

Reference

[1] Vasantharani P, Vichitra SN alias. Structural and Elastic Studies of Strontium Doped Manganese Borate Glasses. IOSR Journal of Applied Physics 2017;09. https://doi.org/10.9790/4861-0904014449.

[2] D V, C D, Deka U. A comprehensive review of structural, and optical properties of boronated glasses doped with 3-d transition metal oxides (TMOs). J Alloys Compd 2025;1024:180145. https://doi.org/10.1016/J.JALLCOM.2025.180145.

[3] Aktas B, Yalcin S, Albaskara M, Aytar E, Ceyhan G, Turhan ZŞ. Effect of Er2O3 on structural, mechanical, and optical properties of Al2O3-Na2O-B2O3-SiO2 glass. J Non Cryst Solids 2022;584:121516. https://doi.org/10.1016/j.jnoncrysol.2022.121516.

[4] Aktas B, Yalcin S, Dogru K, Uzunoglu Z, Yilmaz D. Structural and radiation shielding properties of chromium oxide doped borosilicate glass. Radiation Physics and Chemistry 2019;156:144–9. https://doi.org/10.1016/j.radphyschem.2018.11.012.

[5] Devaraja C, Gowda GVJ, Keshavamurthy K, Eraiah B. The optical and physical properties of holmium (Ho3+) ions doped bismuth-tellurite glasses. AIP Conf. Proc., vol. 2162, 2019. https://doi.org/10.1063/1.5130382.

[6] Brauer DS, Möncke D. Introduction to the Structure of Silicate, Phosphate and Borate Glasses. RSC Smart Materials 2016;2017-January:61–88. https://doi.org/10.1039/9781782622017-00061.

[7] Shiva Kumar BN, Vinay D. Effect of cerium oxide on physical, structural, and spectroscopic properties of tellurium-borate glasses for cool greenish light emitting devices. Scientific Reports 2026 2026. https://doi.org/10.1038/s41598-026-40883-y.

[8] Gomaa HM, Moneep AM, Abdel-Moety AS, Bendary AA, Yahia IS, Zyoud SH. Influence of incorporation of Fe2O3 content on the structural and the dielectric relaxation properties of lithium boro-vanadate oxide glass: toward ideal cathode glasses. Appl Phys A Mater Sci Process 2023;129. https://doi.org/10.1007/S00339-022-06350-X.

[9] Zhang H, Lin H, Yang A, Wang P, Zhang X, Gao P, et al. Luminescence properties of chalcohalide devitrified glass containing BaCl2:Tm3+,Er3+ nanocrystals. J Lumin 2024;273:120688. https://doi.org/10.1016/J.JLUMIN.2024.120688.

[10] Arya SK, Chhina MK, Choudhary R, Dua V, Singh K. Growth of different nanocrystalline phases in ZnO–Li2O–B2O3–TiO2–V2O5 glass and their effect on photoluminescence and photocatalytic activity. Ceram Int 2022;48. https://doi.org/10.1016/j.ceramint.2022.04.030.

[11] Bengisu M. Borate glasses for scientific and industrial applications: a review. J Mater Sci 2016;51. https://doi.org/10.1007/s10853-015-9537-4.

[12] Liang H, Yang G, Zhang M, Zhou D, Xia F, Etschmann BE, et al. High performing ferrous ion-doped phosphosilicate glass for energy-efficient windows. Chemical Engineering Journal 2025;511:161985. https://doi.org/10.1016/J.CEJ.2025.161985.

[13] D'Silva AJ, Maheshvaran K, Rayappan IA. Influence of alkali and alkaline-earth metal oxides on Sm3+ ions-doped borate glasses: synthesis, structural, and optical investigations for reddish-orange solid-state-lighting applications. Journal of Materials Science: Materials in Electronics 2024;35:1630. https://doi.org/10.1007/s10854-024-13368-9.

[14] Obayes HK, Wagiran H, Hussin R, Saeed MA. Structural and optical properties of strontium/copper co-doped lithium borate glass system.

Mater Des 2016;94:121–31. https://doi.org/10.1016/J.MATDES.2016.01.018.

[15] Guntu RK, Ashok P, Sivaram K, Shetty PB, Babu S, Israr M. Investigations on thermoluminescence, photoluminescence and radiation shielding properties of Dy2O3 doped Li2O-Al2O3-SiO2-Y2O3 glasses for thermoluminescent dosimeter applications. Applied Physics A 2025 131:9 2025;131:701-. https://doi.org/10.1007/s00339-025-08757-8.

[16] Shelby JE. Introduction to Glass Science and Technology. Introduction to Glass Science and Technology 2020. https://doi.org/10.1039/9781839169229.

[17] Sayer M, Mansingh A. OXIDE GLASSES. Noncryst Semicond 2002:463–511. https://doi.org/10.1016/B978-008043958-7/50030-3.

[18] Graça MPF, Melo BMG, Prezas PR, Valente MA, Freire FNA, Bih L. Electrical and dielectric analysis of phosphate based glasses doped with alkali oxides. Mater Des 2015;86:427–35. https://doi.org/10.1016/J.MATDES.2015.07.043.

[19] Varshneya AK, Mauro JC. Composition-structure-property relationship principles. Fundamentals of Inorganic Glasses 2019:165–72. https://doi.org/10.1016/B978-0-12-816225-5.00006-7.

[20] Karmakar B. Fundamentals of Glass and Glass Nanocomposites. Glass Nanocomposites: Synthesis, Properties and Applications 2016:3–53. https://doi.org/10.1016/B978-0-323-39309-6.00001-8.

[21] Roopa, Eraiah B. Experimental and theoretical approach on the physical, structural and optical properties of ZrO2 - Na2O - B2O3 glasses doped with Dy2O3. J Non Cryst Solids 2021;551:120394. https://doi.org/10.1016/J.JNONCRYSOL.2020.120394.

[22] Srinivasa Rao L, Aruna Prabha K, Naidu CD, Hussain S. Structural aspects of Bi2O3–B2O3–MnO2–ZrO2 glasses evaluated by Raman and photoluminescence spectroscopy for solid state lighting. Inorg Chem

Commun 2025;173:113787. https://doi.org/10.1016/J.INOCHE.2024.113787.

[23] Gomaa HM, Saudi HA, Elkatlawy SM, Yahia IS, Makram BMA, Zahran HY. Structure and electrical properties of some Fe-doped sodium borate devitrified glasses: self-heating action. Appl Phys A Mater Sci Process 2023;129. https://doi.org/10.1007/S00339-023-06605-1.

[24] Bhogi A, Kistaiah P. Spectroscopic properties of alkali alkaline earth borate glasses doped with Fe3+ ions. Journal of the Australian Ceramic Society 2020;56. https://doi.org/10.1007/s41779-019-00426-3.

[25] Huang Q, Liu T, Shen X, Li X, Lu A, Gu Y. Characterization of Fe2O3 doping on structure, optical and luminescence properties of magnesium aluminosilicate-based glasses. J Non Cryst Solids 2021;563. https://doi.org/10.1016/j.jnoncrysol.2021.120786.

[26] Pattar V, Rajashekara KM, Devaraja C, Kaewkhao J, Surzhikova DP, Rajanavaneethakrishna R. Investigation of structural, physical and optical properties of sodium boro-tellurite glasses doped with iron oxide. Ceram Int 2024;50:30434–44. https://doi.org/10.1016/J.CERAMINT.2024.05.341.

[27] Xu Y, Liao Q, Wang F, Gu Y, Pu B, Zhu H. Effect of Fe2O3 on the structure and properties of Mo-containing borosilicate glasses for nuclear waste immobilization. Int J Appl Glass Sci 2025;16:e16680. https://doi.org/https://doi.org/10.1111/ijag.16680.

[28] Khan S, Kaur G, Singh K. Effect of ZrO2 on dielectric, optical and structural properties of yttrium calcium borosilicate glasses. Ceram Int 2017;43. https://doi.org/10.1016/j.ceramint.2016.09.219.

[29] Kumar D, Rao SM, Singh SP. Structural, optical and thermoluminescence study of Dy3 + ion doped sodium strontium borate glass. J Non Cryst Solids 2017;464. https://doi.org/10.1016/j.jnoncrysol.2017.03.029.

[30] Aqdim S, Naji M, Chakir A, Bouari A El. Design, synthesis and structural properties of borate glasses: Towards an alkali-free bioactive glass. J Non Cryst Solids 2022;597. https://doi.org/10.1016/j.jnoncrysol.2022.121876.

[31] Kilic G, Ilik E, Mahmoud KA, El-Agawany FI, Alomairy S, Rammah YS. The role of B2O3 on the structural, thermal, and radiation protection efficacy of vanadium phosphate glasses. Appl Phys A Mater Sci Process 2021;127. https://doi.org/10.1007/s00339-021-04409-9.

[32] Mirkazemi M, Marghussian VK, Beitollahi A, Dou SX, Wexler D, Konstantinov K. Effect of ZrO2 nucleant on crystallisation behaviour, microstructure and magnetic properties of BaO-Fe2O3-B2O3-SiO2 glass ceramics. Ceram Int 2007;33. https://doi.org/10.1016/j.ceramint.2005.10.011.

[33] Hovington P, Timoshevskii V, Burgess S, Demers H, Statham P, Gauvin R, et al. Can we detect Li K X-ray in lithium compounds using energy dispersive spectroscopy? Scanning 2016;38. https://doi.org/10.1002/sca.21302.

[34] Rohilla R, Khasa S, Hooda A. Structural and impedance spectroscopic investigations of eco-friendly alkali phosphoborate glass–ceramics containing zirconium ion. Environmental Science and Pollution Research 2023;30. https://doi.org/10.1007/s11356-022-21867-7.

[35] Design and evaluation of TiO2-enhanced phosphate glasses for dual-functionality: Photonic applications and radiation safety. Physica B Condens Matter 2025;716:417735. https://doi.org/10.1016/J.PHYSB.2025.417735.

[36] Usman I, Sanusi MSM, Ahmad NE, Shafiq bin Shaharin M. Structural and optical properties of tungsten-sodium-zinc-borate glass doped α-Fe2O3 nanoparticle. Ceram Int 2023;49:26256–66. https://doi.org/10.1016/J.CERAMINT.2023.05.079.

[37] Vamshi Babu K, Chanakya N, Aravind S, Upender G. Structural, Thermal, Optical and DC Conductivity Studies of 30TeO2-40B2O3-(30-x)BaO-xNa2O (0 ≤ x ≤ 30 mol%) Glass System. J Inorg Organomet Polym Mater 2023. https://doi.org/10.1007/s10904-023-02914-3.

[38] Shiva Kumar B.N., Devaraja C., R.S. Gedam, Eraiah B., Jagadeesha Gowda G.V., Harisha G., et al. Implications of silver nitrate doping on the physical, structural, and optical attributes of Na2O−ZnO−Borate glasses. J Mol Struct 2025;1325:140985. https://doi.org/10.1016/J.MOLSTRUC.2024.140985.

[39] El-Moneim AA, Ahmed RM, Sallam OI, El-Mallawany R. Physical, structural and elastic properties of Fe2O3-doped oxyfluoroborate glasses. Appl Phys A Mater Sci Process 2025;131:1–14. https://doi.org/10.1007/S00339-025-08247-X/FIGURES/13.

[40] Sayyed MI, Abdo MA, Elhosiny Ali H, Sadeq MS. Fe2O3 within Na2O–Al2O3– B2O3 glasses to study the structural and optical features changes. Opt Mater (Amst) 2022;131. https://doi.org/10.1016/j.optmat.2022.112419.

[41] Al-Ghamdi H, Alsaif NAM, Afaneh F, El-Refaey AM, Elsad RA, Shams MS, et al. Effect of iron ion doping on mechanical, dielectric properties, and radiation protection effectiveness of lead barium borate glasses. Appl Phys A Mater Sci Process 2024;130. https://doi.org/10.1007/s00339-023-07168-x.

[42] Vinay D, Shiva Kumar B. N, Siddalingeshwara B P, Meher Taj S, D R Rangaswamy, Ashok Reddy G.V, et al. Silver oxide embedded alkali zinc boro tellurite glasses: Physical, structural and optical properties for possible optical switching applications. J Mol Struct 2025;1339:142388. https://doi.org/10.1016/J.MOLSTRUC.2025.142388.

[43] Devaraja C, Jagadeesha Gowda G V., Eraiah B, Keshavamurthy K. FTIR and Raman studies of Eu3+ ions doped alkali boro tellurite

glasses. AIP Conf. Proc., vol. 2115, 2019. https://doi.org/10.1063/1.5113069.

[44] Abdel Wahab EA, Shaaban KS, Yousef ES. Enhancement of optical and mechanical properties of sodium silicate glasses using zirconia. Opt Quantum Electron 2020;52. https://doi.org/10.1007/s11082-020-02575-3.

[45] Bhogi A, Pothuganti PK, Kistaiah P. Structural properties of Li2O-BaO-B2O3-Fe2O3glasses. AIP Conf Proc 2020;2220. https://doi.org/10.1063/5.0001158/890125.

[46] Abdel-Aziz AM, Shams MS, Ahmed EM, Rammah YS, Elsad RA. Fabrication, physical, FTIR, ultrasonic waves, and mechanical properties of quaternary B2O3–Bi2O3–NaF–ZrO2 glasses: Experimental study. Appl Phys A Mater Sci Process 2022;128. https://doi.org/10.1007/s00339-022-05732-5.

[47] Budida J, Rao CS, Chand NR, Guntu RK. Spectral and Structural Tailoring of Sm2O3-Doped LiF-La2O3-PbO-B2O3 Glasses for Advanced Luminescent Devices. Journal of Electronic Materials 2025 54:11 2025;54:10611–47. https://doi.org/10.1007/s11664-025-12286-8.

[48] Hassaan MY, Bendary AA, Abdel-Wahed MH, Atta MR, Abdel-Moety AS. Influence of ZrO2 additions on the structural and optical properties of Na-B-Te Glass for Optoelectronic Applications. Journal of the Egyptian Society for Basic Sciences-Physics 2025;2:16–22. https://doi.org/10.21608/JESBSP.2025.315233.1024.

[49] Kamitsos EI, Karakassides MA, Chryssikos GD. Vibrational spectra of magnesium-sodium-borate glasses. 2. Raman and mid-infrared investigation of the network structure. Journal of Physical Chemistry 1987;91:1073–9. https://doi.org/10.1021/J100289A014/SUPPL_FILE/J100289A014_SI_001.PDF.

[50] Siddalingeshwara BP, Sabari Girisun TC, Abith M, Devaraja C, Sivasankara Reddy N, Anil Kumar GN. Structural correlation to linear and non-linear optical properties of Bi3+ ion doped Li2O–SrO–B2O3 glasses: Optical switching and limiting applications. Ceram Int 2024;50:37880–99. https://doi.org/10.1016/J.CERAMINT.2024.07.151.

[51] Ardelean I, Toderas M, Păşcuţă P. Structural study of the Fe2O3-B2O 3-BaO glass system by FTIR spectroscopy. Modern Physics Letters B 2003;17. https://doi.org/10.1142/S0217984903006098.

[52] Varsamis CPE, Makris N, Valvi C, Kamitsos EI. Short-range structure, the role of bismuth and property-structure correlations in bismuth borate glasses. Physical Chemistry Chemical Physics 2021;23. https://doi.org/10.1039/d1cp00301a.

[53] Möncke D, Kamitsos EI, Palles D, Limbach R, Winterstein-Beckmann A, Honma T, et al. Transition and post-transition metal ions in borate glasses: Borate ligand speciation, cluster formation, and their effect on glass transition and mechanical properties. Journal of Chemical Physics 2016;145. https://doi.org/10.1063/1.4962323.

[54] Vinay D, Devaraja C, R. S. Gedam, Eraiah B, G. V. Jagadeesha Gowda, Ashok Reddy G. V, et al. Investigation of physical, structural, optical, and luminescence properties of nickel oxide doped alkali zinco-borate glasses. Scientific Reports 2025 15:1 2025;15:1–20. https://doi.org/10.1038/s41598-025-91852-w.

[55] Kaky KM, Lakshminarayana G, Baki SO, Taufiq-Yap YH, Kityk I V., Mahdi MA. Structural, thermal, and optical analysis of zinc boro-aluminosilicate glasses containing different alkali and alkaline modifier ions. J Non Cryst Solids 2017;456. https://doi.org/10.1016/j.jnoncrysol.2016.10.044.

[56] Srinivasa Rao L, Aruna Prabha K, Naidu CD, Hussain S. Structural aspects of Bi2O3–B2O3–MnO2–ZrO2 glasses evaluated by Raman and photoluminescence spectroscopy for solid state lighting. Inorg Chem

Commun 2025;173:113787. https://doi.org/10.1016/J.INOCHE.2024.113787.

[57] Vignarooban K, Skipper C, Welton A, Boolchand P. Linking the ring-morphology of (Li2O)x(B2O3)100-x and (Na2O)x(B2O3)100-x borate glasses with topological phases and melt dynamics. J Non Cryst Solids 2025;654:123450. https://doi.org/https://doi.org/10.1016/j.jnoncrysol.2025.123450.

[58] Meera BN, Ramakrishna J. Raman spectral studies of borate glasses. J Non Cryst Solids 1993;159:1. https://doi.org/10.1016/0022-3093(93)91277-A.

[59] Ashok K, Yuganand N, Guntu RK, Daniel Francis E. Raman deconvolution, radiation shielding, TL effective and dielectric investigations of Dy3+ doped alumina lead borate glasses. Radiation Physics and Chemistry 2024;224:112057. https://doi.org/10.1016/J.RADPHYSCHEM.2024.112057.

[60] Hivrekar MM, Sable DB, Solunke MB, Jadhav KM. Network structure analysis of modifier CdO doped sodium borate glass using FTIR and Raman spectroscopy. J Non Cryst Solids 2017;474:58–65. https://doi.org/10.1016/J.JNONCRYSOL.2017.08.028.

[61] Abdel-Ghany AM, Abu-Khadra AS, Sadeq MS. Influence of Fe cations on the structural and optical properties of alkali-alkaline borate glasses. J Non Cryst Solids 2020;548:120320. https://doi.org/10.1016/J.JNONCRYSOL.2020.120320.

[62] Sadeq MS, Sayyed MI, Mahmoud AE razek, Abdo MA, Ali HE, Morshidy HY. Composition dependence of transparency, optical, ligand field and radiation shielding properties in CdO–Fe2O3–Na2O–B2O3 glasses. Ceram Int 2023;49. https://doi.org/10.1016/j.ceramint.2023.06.071.

[63] Jagadeesha Gowda G V., Devendra BK, Ashok Reddy G V., Maruthi G, Manjunatha M, Harisha G, et al. STRUCTURAL, PHYSICAL, AND

OPTICAL PROPERTIES OF LEAD BORO-TELLURITE GLASSES DOPED WITH EUROPIUM TRIOXIDE. Rasayan Journal of Chemistry 2023;16:692. https://doi.org/10.31788/RJC.2023.1628300.

[64] Gowda GVJ, Deka U, Dahshan A, Reddy GVA, Eraiah B, Gedam RS, et al. Exploration of physical, structural, thermal, and optical properties of alkali zinc boro tellurite glasses doped with europium trioxide. Appl Phys A Mater Sci Process 2024;130:1–15. https://doi.org/10.1007/S00339-024-07920-X/FIGURES/18.

[65] Siddalingeshwara BP, Sivasankara Reddy · N, Jagannathan · Abhiram. The effect of NiO on the structural and optical properties of lithium strontium borate glasses. Journal of Optics 2024 2024:1–13. https://doi.org/10.1007/S12596-024-02008-4.

[66] Abdel Wahab EA, Shaaban KS. Structural and optical features of aluminum lead borate glass doped with Fe2O3. Appl Phys A Mater Sci Process 2021;127:1–12. https://doi.org/10.1007/S00339-021-05062-Y/FIGURES/11.

[67] Dimitrov V, Komatsu T. Classification of Simple Oxides: A Polarizability Approach. J Solid State Chem 2002;163:100–12. https://doi.org/10.1006/JSSC.2001.9378.

[68] Gowda GVJ, Reddy GVA, Eraiah B, Devaraja CR. Investigations of structural modifications, physical and optical properties of lead boro-tellurite glasses doped with europium trioxide for possible optical switching applications. Journal of Metals, Materials and Minerals 2023;33. https://doi.org/10.55713/jmmm.v33i2.1610.

[69] Umar SA, S.N N, Geidam IG, El-Mallawany R, M. Abd-Elnaiem A, Hakamy A, et al. Optical basicity, polarizability and spectroscopic investigations of CuO doped TeO2–B2O3 glass system. Mater Chem Phys 2023;297:127309. https://doi.org/10.1016/J.MATCHEMPHYS.2023.127309.

[70] Abul-Magd AA, Abu-Khadra AS, Abdel-Ghany AM. Physical, thermal, optical, shielding and elastic properties of Bi2O3–B2O3–TeO2 glass system doped with Fe2O3. Radiation Physics and Chemistry 2024;217:111444. https://doi.org/10.1016/j.ceramint.2021.03.326.

[71] Fattah Khedr AA, Abul-Magd AA. Tuning the optical band gap and shielding efficiency of heavy metal borate glasses through controlled Fe2O3 doping. Opt Mater (Amst) 2025;160:116717. https://doi.org/10.1016/J.OPTMAT.2025.116717.

[72] Tichá H, Tichý L. Semiempirical relation between non-linear susceptibility (refractive index), linear refractive index and optical gap and its application to amorphous chalcogenides. Journal of Optoelectronics and Advanced Materials 2002;4.

[73] Doddoji R, Meejitpaisan P, Kaewkhao J. Determination of optical constants via the single oscillator Drude-Voigt dispersion model in fluoroborate glass for optical lenses: Nonlinear optical properties. Physica B Condens Matter 2023;671. https://doi.org/10.1016/j.physb.2023.415398.

[74] El-Sayed MA, Alfryyan N, Alsaif NAM, Al-Ghamdi H, Abouhaswa AS, Abdelghany AM, et al. A detailed analysis of linear/nonlinear optical properties of boro-tellurite glasses reinforced with ZrO2 for optoelectronics applications. Appl Phys A Mater Sci Process 2025;131:1–11. https://doi.org/10.1007/S00339-025-08386-1/FIGURES/9.

[75] Sorkhabi SY, Rezvani M, Oskoui PR. Effects of Fe2O3 and CuO on structural, thermal and optical properties of P2O5-ZnO-Na2O glass system. Results in Optics 2025;18:100779. https://doi.org/10.1016/j.rio.2025.100779.

[76] Aloraini DA, Almuqrin A, Albarzan B, Shaaban KS, Wahab EAA. Impact of Fe2O3 on Structural Properties, Nonlinear Optical Behavior, and Radiation Shielding Efficiency of Lead Phosphate

Glasses. JOM 2025 77:12 2025;77:9894–909. https://doi.org/10.1007/s11837-025-07806-0.

[77] Alfryyan N, Alsaif NAM, Al-Ghamdi H, Shaaban SM, Shams MS, El-Refaey AM, et al. Structural, Physical, Optical Properties as well γ-ray Attenuation Capability of Bismuth Borate Containing Fe2O3 and CuO: Potential Use in Optical and Radiation Shielding Applications. Journal of Materials Engineering and Performance 2025 34:23 2025;34:27749–58. https://doi.org/10.1007/s11665-025-11962-4.

[78] Bawazeer O, Sadeq MS. Compositional dependency of transparency, optical and radiation shielding parameters inside Gd2O3–Fe2O3–Na2O–SiO2–B2O3 glass. Ceram Int 2024;50:159–73. https://doi.org/10.1016/j.ceramint.2023.10.079.

[79] Wang Y, Bu Q, Li D, Yang S, Li L, Xiang G, et al. UV- and X-ray-activated broadband NIR garnet-type Ca3Ga2Sn3O12:Fe3+ phosphors with efficient persistent luminescence. Dyes and Pigments 2024;225. https://doi.org/10.1016/j.dyepig.2024.112091.

[80] Alyabyeva L, Burkov V, Mill B. Optical spectroscopy of La3Ga5SiO14 disordered crystals doped with Fe3+ ions. Opt Mater (Amst) 2015;43. https://doi.org/10.1016/j.optmat.2015.02.023.

[81] Wei Y, Xing G, Liu K, Li G, Dang P, Liang S, et al. New strategy for designing orangish-red-emitting phosphor via oxygen-vacancy-induced electronic localization. Light Sci Appl 2019;8. https://doi.org/10.1038/s41377-019-0126-1.

[82] McCamy CS. Correlated color temperature as an explicit function of chromaticity coordinates. Color Res Appl 1992;17. https://doi.org/10.1002/col.5080170211.

[83] Pawar PP, Gedam RS, Agarwal K. Insight into the physical, structural, thermal and spectroscopic characteristics of intense green luminescent Tb3+ incorporated lithium alumino-borate glasses for

green LED application. J Mol Struct 2025;1340:142523. https://doi.org/10.1016/j.molstruc.2025.142523.

[84] Chen Q, Chen L, Feng Y, Gao T, Huang T. KBiFe2O5 triggered-phase transition of Bi2Fe4O9 and Fe3O4 in tellurite glass with huge nonlinear and magnetic properties. Ceram Int 2025;51:2737–55. https://doi.org/10.1016/J.CERAMINT.2024.05.383.